UNIVERSITY OF OKLAHOMA

GRADUATE COLLEGE

QUANTUM MONTE CARLO STUDY OF BOSONIC LATTICE SYSTEMS IN THE PRESENCE OF DISORDER

A DISSERTATION

SUBMITTED TO THE GRADUATE FACULTY

in partial fulfillment of the requirements for the

Degree of

DOCTOR OF PHILOSOPHY

By

CHAO ZHANG
Norman, Oklahoma
2018

QUANTUM MONTE CARLO STUDY OF BOSONIC LATTICE SYSTEMS IN THE PRESENCE OF DISORDER

A DISSERTATION APPROVED FOR THE
HOMER L. DODGE DEPARTMENT OF PHYSICS AND ASTRONOMY

BY

Dr. Bruno Uchoa, Chair

Dr. Doerte Blume

Dr. Arne Schwettmann

Dr. Barbara Capogrosso-Sansone

Dr. Henry Neeman

DEDICATION

to

My loving children, Alice and Bob

My husband, Jin

Acknowledgements

I would like to thank my advisor Dr. Barbara Capogrosso-Sansone for her guidance, support, and encouragement during my Ph.D. study. Without her guidance and persistent help, this dissertation would not have been possible. I would like to thank my committee members, Professor Bruno Uchoa, Professor Doerte Blume, Professor Arne Schwettmann, and Professor Henry Neeman, for their advice and encouragement in my academic career. I also thank Professor Deborah Watson and Professor Kieran Mullen for their encouragement during the last several years.

I deeply thank my parents, Xuen Zhang and Meiling Wu, for taking care of my babies. Without their help, I could not have finished my Ph.D. with two lovely children. I also need to thank my two lovely children: Alice and Bob, they give me endless happiness.

Finally and most importantly, I thank my husband Jin Yang, for always being with me, supporting me, and understanding me.

Table of Contents

List of Figures

Abstract

Disorder is ubiquitous in condensed matter systems, but a thorough understanding of these systems is hindered by poor control over the nature of disorder and competing interactions. Ultracold gases trapped in optical lattices, on the other hand, offer an unprecedented level of control over interactions and disorder, and are ideal candidates to test theoretical predictions and study fascinating phenomena resulting from the interplay between disorder, interaction, and quantum degeneracy.

In this dissertation, I present my research on strongly correlated many-body lattice bosons in the presence of disordered potentials. My results are based on quantum Monte Carlo simulations by the Worm algorithm. Experimentally, lattice bosons can be realized by ultracold gases in optical lattices. I studied the ground state phase diagram of the above systems in the presence of diagonal (quasi-periodic disordered potential or random disordered potential) and off-diagonal disorder (in the form of site dilution).

First, I will discuss the ground state phase diagram of two-dimensional bosons in quasi-periodic lattices. Then, I will discuss the phase diagram as well as finite temperature thermodynamic properties of two-dimensional dipolar lattice bosons in the presence of random diagonal disordered potentials. Finally, I will discuss the phase diagram of two-dimensional hard-core lattice bosons system in the presence of long-range hopping and long-range two-body interactions both in the absence of disorder and in the presence of site dilution (equivalent to off-diagonal

disorder). This system is equivalent to the long-range XXZ model as realized by polar molecules trapped in a deep optical lattice. These results provide theoretical guidance for experimentalists to find quantum phase transitions as well as exotic quantum phases in strongly correlated bosonic lattice systems.

Chapter 1

Introduction

Disordered systems are ubiquitous in many areas of physics, including condensed matter physics, optics, acoustics, seismology, and atomic physics. The effect of disorder in condensed matter systems has been thoroughly studied since the discovery of Anderson localization for non-interacting systems. This phenomenon is named after P. W. Anderson, who was the first to find that free fermions can be localized in the presence of random disordered potentials [9]. The combined effects of disorder and interactions are very rich, given that they depend on the nature of the system (fermions or bosons, such as cooper pairs in a superconductor for fermionic systems or superfluidity for bosonic systems) and on the dimension of the system. Many experiments on disordered systems, such as films of ^{4}He adsorbed on substrates [10, 11], bosonic magnets [12, 13, 14], Josephson junction arrays [15], and thin superconducting films [16, 17], have been conducted for decades. However, a thorough understanding of these systems is hindered by poor control over the nature of disorder and competing interactions.

More recently, disorder has been successfully studied with ultracold gases trapped in optical lattices. These systems offer an unprecedented level of control over disorder and interactions, making them ideal candidates to simulate disordered condensed matter systems, test theoretical predictions, and study fascinating phenomena resulting from the interplay between disorder, interaction, and quantum degeneracy. Specifically, in experiments with ultracold gases in optical

lattices, disorder and interactions can be generated and manipulated independently. Random disordered potentials are usually produced using speckle patterns, while quasi-periodic potentials can be generated by bichromatic lattices [18, 19, 20, 21]. The interaction can be a contact interaction as well as a long-range off-site interaction (e.g., dipolar interaction). The contact interaction is a short-range interaction that comes from s-wave scattering, which occurs when two ultracold atoms are within the same lattice site. It can be tuned in experiments by using Feshbach resonances [22, 23, 24, 25, 17, 26, 6, 27, 19, 28, 3, 29]. The dipolar interaction, which has long-range and anisotropic properties, can be realized with ultracold dipolar molecules in optical lattices [30, 31, 32, 33, 34, 35, 36, 37, 38, 39, 40, 41, 42]. Recently, spectacular observation of Anderson localization of matter waves was reported in Ref. [43], and several investigations of the combined effect of disorder and interactions have been or are currently being performed as well [27, 3, 19, 28, 29].

Under certain experimental conditions, ultracold gases trapped in optical lattices can be described by the Bose-Hubbard model [44, 45, 46, 8, 7, 47, 48, 49, 50]. The original Bose-Hubbard model simply contains a kinetic energy term that tends to delocalize particles and an interaction term that tends to localize particles. At zero temperature and integer filling factors, the competition between kinetic energy and interaction drives a quantum phase transition between the Mott insulator (MI) phase and the superfluid (SF) phase. More interestingly, in the presence of a disordered potential, at filling factor $n = 1$, it is proven analytically and confirmed numerically that a new phase, gapless Bose glass (BG) phase, characterized by finite compressibility and the absence of off-diagonal long-range

order, always intervenes between the MI and SF phases [8, 7]. If we go a bit further, taking long-range dipolar interactions into the Bose-Hubbard model, new quantum phases, such as the supersolid phase, the checkerboard (CB) solid phase, and the stripe solid (SS) phase are predicted in theory. By adding disordered potentials in the Bose-Hubbard model with long-range dipolar interactions, at half filling, the interplay of dipolar interactions and on-site disorder leads to suppression of the CB solid phase, enhancement of the SF phase, and stabilization of the BG phase [51].

The work described in this dissertation is devoted to studying strongly interacting bosonic particles in optical lattices in the presence of disorder. It is written based on my work published in references [49], [51], and [52], and is organized as follows. Chapter 2 briefly introduces the Bose-Hubbard model and the MI to SF phase transition. Chapter 3 introduces the Bose-Hubbard model in the presence of random disordered potentials. Here I discuss experimental realization of disordered potentials, Anderson localization in the weakly interacting regime, and the Bose-Hubbard model in the strongly interacting regime. Chapter 4 introduces Monte Carlo method with the Worm algorithm. Chapter 5 systematically studies equilibrium phases of two-dimensional bosons in quasi-periodic lattices. Chapter 6 systematically studies equilibrium phases of dipolar lattice bosons in the presence of random diagonal disordered potentials. Chapter 7 systematically studies equilibrium phases and the disordered case in terms of site dilution of the long-range XXZ spin model. This XXZ spin model can be mapped to hard-core dipolar lattice bosons in the presence of long-range hopping and long-range

two-body interactions. Chapter 8 summarizes and concludes my work.

Chapter 2

Bose-Hubbard model and Mott insulator to superfluid phase transition

In this chapter, I introduce optical lattices, the Bose-Hubbard model, and the Mott insulator to superfluid phase transition. The Bose-Hubbard model is a simple yet effective model to describe weakly interacting bosonic particles trapped in a lattice. The Hamiltonian for the Bose-Hubbard model contains two terms: a kinetic energy term and an on-site interaction term. The kinetic energy term tends to delocalize particles, while the on-site interaction term tends to localize particles. At zero temperature and integer filling factor, the competition of these two terms leads to the Mott insulator to superfluid phase transition. The Bose-Hubbard model is the basic model that will be used in Chapters 5, 6, and 7.

2.1 Optical lattices

When a laser beam is shined on atoms, there are two interactions between the atoms and the laser beam: a dissipative force and a conservative force. The dissipative force comes from the stimulated excitation of atoms when photons are absorbed from the laser beam and then spontaneously emitted. Both the absorption and emission processes give atoms a "kick", a retro-reflected momentum. The difference is that stimulated excitation only happens along the direction of the laser beam, while spontaneous emission happens in random directions. On time average, this dissipative force slows down the motion of the atoms. This is why

it is called a dissipative force. On the other hand, the conservative force can be used independently to trap atoms. When atoms are illuminated with laser beams, the electric fields of the laser beams induce dipole moments in the atoms, which in turn interact with the electric field of the laser beams. This dipole interaction between the atoms and the laser beams can be described by the following [53]:

$$U_{\mathrm{dip}}(\mathbf{r}) = \frac{3\pi c^2}{2\omega_0^3}\frac{\Gamma}{\Delta}I(\mathbf{r}) \quad , \tag{2.1}$$

where c is the speed of light, ω_0 is the transition frequency of the atoms, Γ is the spontaneous decay rate of the excited atomic level, $\Delta = \omega - \omega_0$ is the detuning of the laser frequency, ω is the frequency of the laser beam, and $I(\mathbf{r})$ is the spatial distribution of the laser intensity. Since $U_{\mathrm{dip}}(\mathbf{r}) \sim I(\mathbf{r})$, we can see that the shape of the dipole potential is related to the intensity distribution of the laser beam. For example, a laser beam with an intensity of Gaussian distribution gives a Gaussian distributed dipole potential. Depending on the detuning of laser beams, there are two kinds of dipole potentials. When laser beams are red-detuned, which means the frequency of the laser beam is larger than the transition frequency of the atoms, all atoms tend to stay in place with a higher intensity. When laser beams are blue-detuned, which means the frequency of the laser beam is smaller than the transition frequency of the atoms, all atoms tend to stay in place with a lower intensity.

As the fundamental platform to explore interactions between ultracold atoms and investigate many-body physics, the optical lattice is one kind of sophisticated

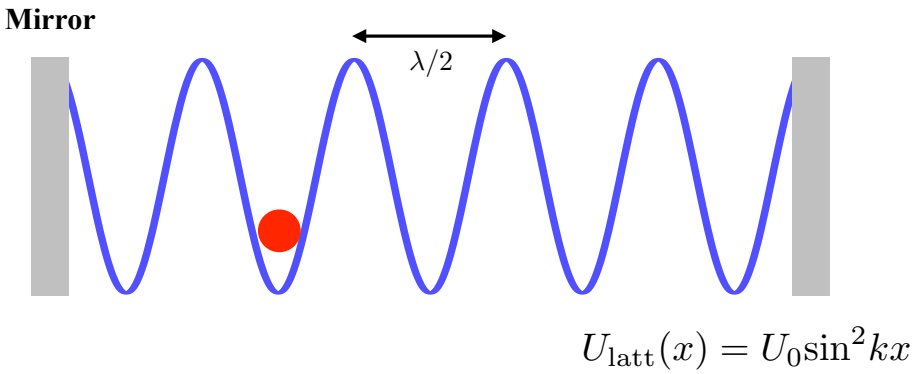

Figure 2.1: Sketch of a 1D optical lattice. The standing electric wave is the result of interference between two counter-propagating laser beams.

dipole trap. When two counter-propagating laser beams with the same frequency and phase are overlapped, we can get a standing wave whose intensity distribution is like a sinusoidal function, as shown in Figure 2.1. In this case, the dipole potential can be described by

$$U_{\mathrm{latt}}(x) = U_0 \sin^2(kx) \quad , \tag{2.2}$$

where U_0 is the U_{dip} in Equation 2.1. It is the dipole potential where we have the maximum intensity. As can be imagined, when atoms are put in this standing wave, all of them tend to stay at the antinodes of the standing wave. These antinodes can be at the highest intensity or at the lowest intensity, depending on whether the laser beams are red-detuned or blue-detuned. A standing wave can be generated by using a mirror to retro-reflect a laser beam. A two-dimensional optical lattice and a three-dimensional lattice can be generated by intersecting

two standing waves or three standing waves perpendicularly. Figure 2.2 shows how to form a three-dimensional optical lattice by using three retro-reflecting laser beams.

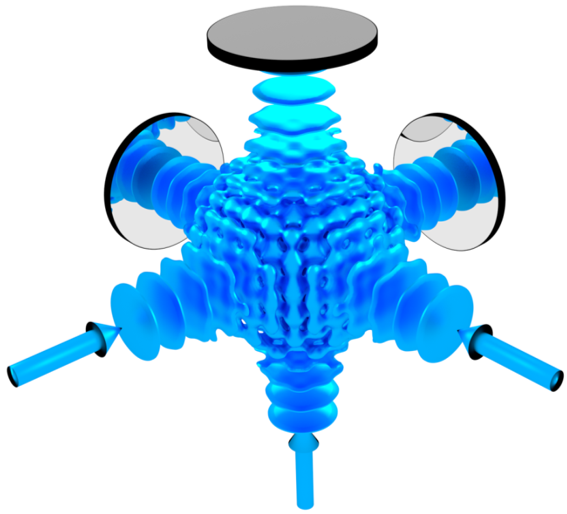

Figure 2.2: The 3D optical lattice structure is formed by using three retro-reflecting laser beams along three directions. This figure is borrowed from the website https://www.amop.phy.cam.ac.uk/Research/MBQD.

The most striking feature of optical lattices is that they can be used to simulate solid state materials. The optical lattice potential mimics the crystal lattice in a solid, and atoms loaded in the optical lattices mimic valence electrons. The movement of atoms in optical lattices can be viewed as the movement of valence electrons in the periodic potential generated by positively charged ions in a solid crystal.

Because optical lattices are formed by intersecting laser beams, the configuration of optical lattices can be fully controlled by tweaking the interference of these laser beams. For example, by changing the intersection angles between laser beams, we can realize hexagonal lattices or square lattices. If we use laser beams

with different wavelengths, we can realize superlattices, such as checkerboard lattices, which allow further control of the atoms. Currently, the optical lattice is such a great tool that it has been used comprehensively in scientific research of quantum computation, quantum simulation, the long-range interaction of atoms and molecules, quantum phase transitions, quantum optics, and so on [54].

2.2 Derivation of the Bose-Hubbard model

In this section, I provide the derivation of the Bose-Hubbard model [55, 56]. Here, we are considering a gas of interacting bosonic particles trapped in the optical lattice.

From the many-body physics point of view, the Hamiltonian of the interacting bosonic particles in the optical lattice with an external trapping potential can be written as

$$\begin{aligned} H_{\text{full}} = \int d\mathbf{r}\Psi^{\dagger}(\mathbf{r})\bigg(-\frac{\hbar^2}{2m}\nabla^2 + V_{\text{latt}}(\mathbf{r}) + V_{\text{T}}(\mathbf{r})\bigg)\Psi(\mathbf{r}) \\ + \frac{1}{2}\int d\mathbf{r}d\mathbf{r}'\Psi^{\dagger}(\mathbf{r})\Psi^{\dagger}(\mathbf{r}')V_{\text{int}}(\mathbf{r}-\mathbf{r}')\Psi(\mathbf{r}')\Psi(\mathbf{r}) \quad , \end{aligned} \tag{2.3}$$

where $\Psi^{\dagger}(\mathbf{r})$ is the bosonic field operator that creates a particle at position $\mathbf{r}$, $\Psi(\mathbf{r})$ is the bosonic field operator that destroys a particle at position $\mathbf{r}$, $V_{\text{latt}}(\mathbf{r})$ is the periodic lattice potential, $V_{\text{T}}(\mathbf{r})$ is the external trapping potential (such as a magnet trap or a harmonic potential), and $V_{\text{int}}(\mathbf{r}-\mathbf{r}')$ is the inter-particle scattering potential. For gases in the sub-millikelvin regime, usually the lowest-angular momentum collisions dominate. Here, we only consider particles interacting via

s-wave scattering, and the inter-particle potential can be replaced with an effective contact interaction:

$$V_{\text{int}}(\mathbf{r}-\mathbf{r}') = \frac{4\pi a_s \hbar^2}{m}\delta(\mathbf{r}-\mathbf{r}') \quad , \tag{2.4}$$

where a_s is the s-wave scattering length and m is the mass of the particle.

In the simplest case, the optical lattice potential in three dimensions takes the form

$$V_{\text{latt}}(\mathbf{r}) = \sum_{i=1}^{3} V_{0i}\sin^2(kx_i) \quad , \tag{2.5}$$

where $k = 2\pi/\lambda$ is the wavevector, λ is the wavelength of the laser beam corresponding to lattice period $a = \lambda/2$, and V_0 is proportional to the intensity of the laser beam.

We assume the energies involved in the system dynamics to be small compared to the excitation energies to the second band. Then, we can expand the field operators in terms of the Wannier functions in the lowest band:

$$\Psi(\mathbf{r}) = \sum_i a_i w_0(\mathbf{r}-\mathbf{r}_i) \quad , \tag{2.6}$$

where $w_0(\mathbf{r}-\mathbf{r}_i)$ is the Wannier function of the lowest band, a_i is the annihilation operator to destroy a particle at site i, and the sum runs over the total number of lattice sites. Then, Equation 2.3 reduces to the Bose-Hubbard Hamiltonian, which describes the system of bosonic particles trapped in an optical lattice with

short-range on-site repulsive interactions:

$$H = -J \sum_{\langle i,j \rangle} {a_i}^\dagger a_j + \frac{U}{2} \sum_i n_i(n_i - 1) + \sum_i \epsilon_i n_i \quad , \tag{2.7}$$

where $\langle i, j \rangle$ denotes the sum over the nearest neighbor pairs, $a_i^\dagger$ and a_i are the bosonic creation and annihilation operators on site i, which obey the canonical commutation relations $[a_i, a_j^\dagger] = \delta_{ij}$, and $n_i = a_i^\dagger a_i$ is the number operator, which gives us the total number of particles on site i. The following definitions hold:

$$J = \int d^3r w_0^*(\mathbf{r} - \mathbf{r}_i) \left(-\frac{\hbar^2}{2m} \nabla^2 + V_{\text{latt}}(\mathbf{r}) \right) w_0(\mathbf{r} - \mathbf{r}_j) \quad , \tag{2.8}$$

$$U = \frac{4\pi a_s \hbar^2}{m} \int d^3r |w_0(\mathbf{r})|^4 \quad , \tag{2.9}$$

$$\epsilon_i = \int d^3r V_{\text{T}}(\mathbf{r}) |w_0(\mathbf{r} - \mathbf{r}_i)|^2 \quad . \tag{2.10}$$

From Equation 2.7, there are three terms in the Hamiltonian: J is the hopping matrix element between nearest neighbors that measures the kinetic energy of the system, U is the on-site repulsive interaction that represents the repulsive interactions among particles occupying the same lattice site, and ϵ_i is the energy offset of each lattice site, which arises from an additional trapping potential.

In the grand canonical ensemble, the total number of particles is not conserved. The Hamiltonian of the Bose-Hubbard model is written as

$$H = -J \sum_{\langle i,j \rangle} {a_i}^\dagger a_j + \frac{U}{2} \sum_i n_i(n_i - 1) - \sum_i \mu_i n_i \quad , \tag{2.11}$$

where $\mu_i = \mu - \epsilon_i$ and μ is the chemical potential.

2.3 Mott insulator to superfluid phase transition

The Hamiltonian of the system described in Equation 2.11, in the absence of external disordered potential, has three terms: a kinetic energy term J, an on-site repulsive interaction potential term U, and a chemical potential term μ. The kinetic energy term tends to delocalize particles, while the potential term tends to localize particles. The kinetic energy term is also called the hopping term. Because particle tends to hop to its nearest neighbors, the energy of the system is lowered. The potential term is also called the on-site repulsive interaction term. Because there is repulsive interaction between two particles when they are occupying the same lattice site, the energy is minimized by suppressing the density fluctuation. The chemical potential term can help us tune the total number of particles in the system. At zero temperature and integer filling factor, the competition between the kinetic energy term and on-site repulsive interaction term leads to the Mott insulator to superfluid phase transition. The Mott insulator phase, characterized by integer (or commensurate) bosonic densities, is a phase with zero compressibility and a gap of particle-hole excitations. The superfluid phase has off-diagonal long-range order and a finite superfluid density.

To understand this Mott insulator to superfluid phase transition, we consider two cases. First, when the on-site interaction potential dominates, which means $U >> J$, the particles are localized in the Mott insulator state, which is shown

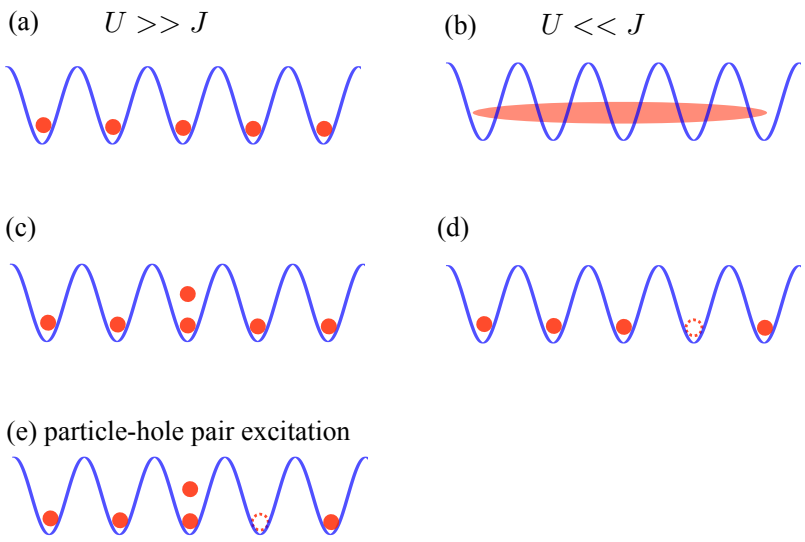

Figure 2.3: A simple picture of bosons trapped in a 1D lattice. (a) The system is in the Mott insulator phase (particles are localized and there is one particle per site). (b) The system is in the superfluid phase (particles are delocalized). (c) One extra particle is added to the system, creating a particle excitation. (d) One particle is removed from the system, creating a hole excitation. (e) Sketch of creating a particle-hole pair in the 1D lattice.

in Figure 2.3(a). For this Mott insulator state, the system is described by using the Fock state, which is approximated by the product of localized wave functions with a fixed number of particles per site. The lowest excitations that conserve the total particle number come from creating particle-hole excitations. A particle-hole excitation means adding one particle to the system plus removing one particle from the system (creating a particle-hole pair in the system). Figure 2.3(e) shows the sketch of creating a particle-hole pair in a one-dimensional lattice. The Mott insulator phase is characterized by zero compressibility and the existence of an energy gap, which is the energy needed to create one particle-hole pair.

As the hopping amplitude J increases, particles are more mobile and have more energy to hop to their nearest neighbors. The second case is that when $J >> U$,

particles try to delocalize among lattice sites. When the ratio J/U reaches a critical value $(J/U)_c$, particle delocalization becomes energetically favorable and the system enters the superfluid phase, which is shown in Figure 2.3(b). The superfluid phase is characterized by finite superfluid density. In the superfluid phase, the system has phase coherence and particles are delocalized among lattice sites.

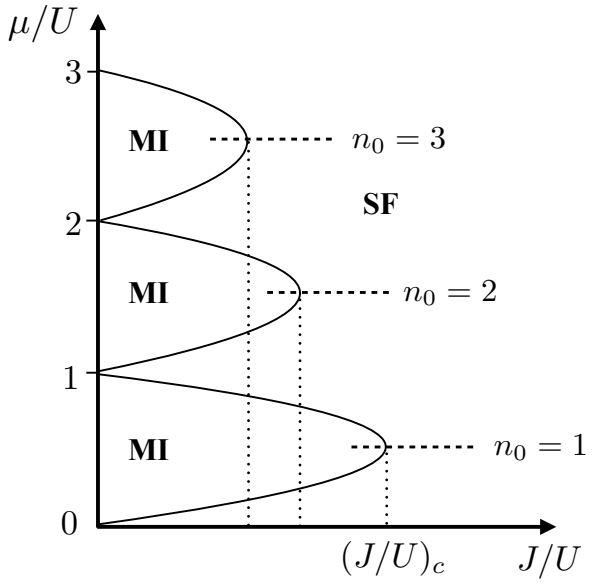

Figure 2.4: Zero-temperature phase diagram for the lattice model of interacting bosons, in the absence of disordered potential. The phase diagram has a lobe shape. There exists one lobe for each integer filling factor n_0. The Mott insulator phase is inside the lobe shape, while the superfluid phase is outside the lobe shape.

Figure 2.4 is the sketch of the phase diagram of the Bose-Hubbard model in μ/U vs. J/U plane, in the absence of disordered potential at zero temperature. The phase diagram has a lobe shape. When the hopping term is much larger than the on-site interaction term, $J >> U$, bosons are delocalized. The system is in the superfluid phase (outside the lobe shape). When the hopping term is much smaller than the on-site interaction term, $J << U$, bosons are localized. The

system is in the Mott insulator phase (inside the lobe shape).

There are two different kinds of transitions in this phase diagram: one is a generic, density-driven transition; the other is a special, multi-critical transition. For the generic density-driven transition, the Mott insulator to superfluid phase transition is driven by adding or removing a small number of particles to or from the Mott insulator state. At fixed J/U, there exists a critical value μ/U at which the kinetic energy gained by adding or removing a particle in or from the system overcomes the potential energy, and the system undergoes the Mott insulator to superfluid phase transition. The elementary excitation of the Mott insulator phase is created by adding or removing particles in or from this system. In this way, particle excitations or hole excitations are created. Figure 2.3(c) shows that there is one extra particle added in the system, creating a particle excitation, and (d) shows that there is one particle removed from the system, creating a hole excitation.

The special transition is driven by the competition between the kinetic energy and the on-site interaction energy. The special transition happens at the tip of the lobe. At the tip of the lobe, the density never changes. At a sufficiently large J/U value, delocalizing quantum fluctuations enables particles to overcome the on-site potential energy, and particles can hop through the whole lattice. The horizontal lines in Figure 2.4 at the tip of the lobe mark the critical value $(J/U)_c$ for the special transition. This special transition belongs to the *d+1* dimensional XY universality class [44].

2.4 Experimental realization of Mott insulator to superfluid phase transition

The Mott insulator to superfluid phase transition has already been observed back in 2002 [1]. For this experimental setup, first, a Bose-Einstein condensate (BEC) is formed by using ^{87}Rb atoms. Then, the BEC is loaded into a three-dimensional optical lattice. After that, the trapping potential of the BEC is turned off and the atomic wave function is expanded freely and interfered with itself. Finally, the interference pattern of the system is observed. In the superfluid phase, particles are delocalized and the system has phase coherence; a high-contrast three-dimensional interference pattern is captured by a CCD camera. It is important to know that the sharp interference maxima directly reflects the high degree of phase coherence in the system, which in turn proves that the system is in the superfluid phase. Figure 2.5 shows the absorption images of multiple matter wave patterns. As can be seen in Figure 2.5(b) and (c), at a potential depth of 3 E_R and 7 E_R (E_R is the recoil energy), the high-contrast three-dimensional interference patterns are clearly observed.

Next, the optical lattice depth is increased. By increasing the depth of the optical lattice, the hopping of these atoms is suppressed and the interference pattern changes remarkably. As shown in Figure 2.5(e), when the depth of the optical lattice increases around 13 E_R, the interference maxima no longer increases in strength. At the same time, the incoherent background of atoms gains more and more strength. At a potential depth around 22 E_R, the interference pattern

is completely lost, which means phase coherence has been completely lost and the system is in the Mott insulator phase. In the Mott insulator phase, atoms are localized and the system has lost phase coherence. By increasing the depth of the optical lattice and recording the interference pattern of the system, the superfluid to Mott insulator phase transition has been observed.

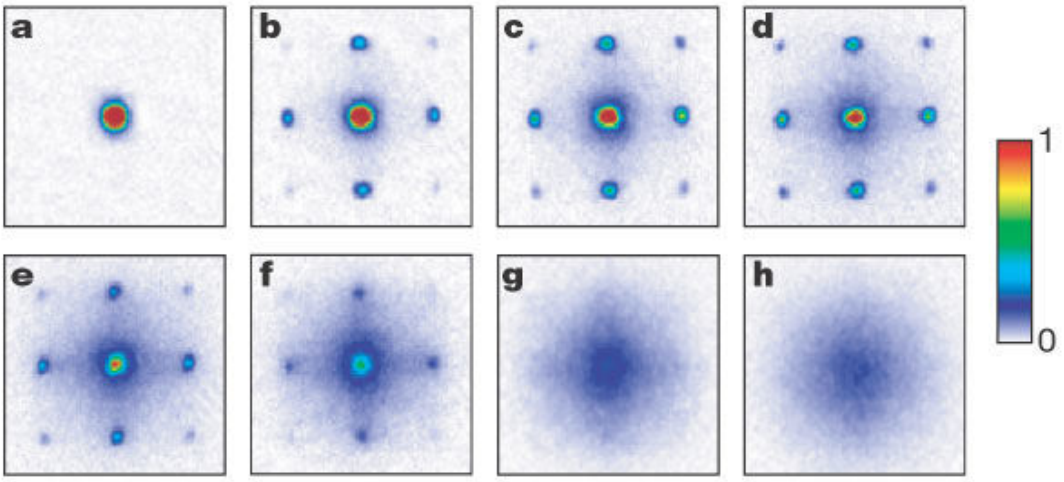

Figure 2.5: The absorption images of multiple matter wave patterns. These were obtained after suddenly releasing atoms from an optical lattice potential with different potential depths V_0 after a time of flight of 15 ms. Values of V_0 were: a, 0 E_R; b, 3 E_R; c, 7 E_R; d, 10 E_R; e, 13 E_R; f, 14 E_R; g, 16 E_R; and h, 20 E_R. The color bar represents relative optical density. This figure is borrowed from Ref. [1].

Chapter 3

Bose-Hubbard model with disordered potential

3.1 Introduction

Disorder or randomness in physical systems has been the focus of research in recent decades. Disorder is an intrinsic property of all real physical systems. For solid state systems, disorder or randomness is shown as vacancies and impurity atoms in the crystal, which are inevitable. The crystal lattice also has defects, such as grain boundaries and disordered structures. The impurities and defects in the crystal, as disorder or randomness, affect the property of solid state systems.

Despite the very broad interest in understanding the physics of disorder in solid state systems, there are still many questions unanswered even from a theoretical point of view. The problem is that disorder cannot be treated in a perturbative way: even a little bit of disorder can produce dramatic changes in physical systems. More than fifty years ago, Anderson first found that free electrons or fermions can be localized in a random disordered potential [9]. From then on, many researchers have investigated the role of disordered potentials in condensed matter systems. They found that disordered potentials tend to localize particles in the system. Originally, Anderson localization is about non-interacting particles. However, real quantum systems have interactions between particles. When we are considering real quantum particles with interactions among them, physical phenomena become more complicated. For example, there is the repulsive Coulomb force, which is

a repulsive long-range interaction between two electrons. For ultracold neutral atoms, the only interaction considered in research comes from s-wave elastic collisions, which are short-range interactions and can be either attractive or repulsive.

One main reason why the combination of disorder and interaction between particles attracts so much attention is that interacting potentials have different behaviors in different regimes. In the non-interacting regime, disorder tends to localize particles. The competition of disorder and kinetic energy induces the phenomenon of Anderson localization. In the weakly interacting regime, the repulsive interactions can compete with disorder and eventually destroy localization. In the strongly interacting regime, strong interactions tend to localize particles. The combination of disorder and interaction leads to an insulator-superfluid (superconductor) phase transition. For instance, when both random disorder and interaction are added to paradigmatic condensed matter models, such as the Bose-Hubbard model or the Bardeen-Cooper-Schrieffer (BCS) model for superconductivity, it gives rise to a disorder-driven phase transition from a conducting phase to an insulating phase, resulting from the localization of bosons or cooper pairs, respectively [44, 57, 58, 59]. Disorder-driven phase transitions have been observed in a wide range of experimental systems such as films of ^{4}He adsorbed on substrates [10, 11], bosonic magnets [12, 13, 14], and thin superconducting films [16, 17]. Despite a remarkable theoretical effort [60, 61, 62, 63, 64, 65, 66, 67], a thorough understanding of the effects of disorder in condensed matter systems is still lacking. That is because, on the one hand,

these systems are challenging to study theoretically; on the other hand, poor control over experimental condensed matter systems does not allow for a thorough experimental investigation of the above systems.

Optical lattice systems of ultracold atoms and molecules provide a possible way to engineer condensed matter systems with an unprecedented level of control and flexibility. Optical lattices mimic the structure of the crystals in solid state systems, while atoms are trapped in an optical lattice mimic valence electrons in the crystal. By using optical lattice systems, all of the parameters entering the Hamiltonian can be tuned in an experiment [54, 68, 69, 2]. Hence, ultracold atoms in optical lattices have rapidly become an important tool in the study of solid state systems.

As I have mentioned previously, disordered structures and defects are inevitable in real solid state systems. As the optical lattice systems of ultracold atoms and molecules become important to the engineering of solid state systems, investigating disordered quantum systems in the optical lattice can give us insight into disordered solid state systems. For optical lattice systems of ultracold atom experiments, random disordered or quasi-periodic disordered potentials can be created using speckle patterns or bichromatic optical lattices, respectively [18, 21, 19, 20]. Speckle patterns are created when light is reflected off a rough surface or travels through a diffusive medium. Quasi-periodic disordered potentials can be created by using a bichromatic lattice, which is formed by combining two optical lattices with incommensurate wavelengths [21]. These two techniques were employed in the first realizations of Anderson localization in one dimension, using non-interacting

bosons in continuum [43] and in an optical lattice [6].

In this chapter, I introduce the experimental realizations of disordered potentials. Then I present Anderson localization as first described by P. W. Anderson in 1958 [9]. In the non-interacting regime, physical phenomena of non-interacting fermions in random disordered potentials are described by Anderson localization. Anderson localization of non-interacting particles has been realized in experiments in the presence of random disordered potentials or quasi-periodic disordered potentials [5, 6].

In the strongly interacting regime, the behavior of strongly interacting systems in the presence of random disordered potentials has been studied extensively, using a variety of theoretical methods [57, 46, 45, 70, 8, 7, 47, 50, 71, 48]. For the most part, these studies have considered systems of bosonic particles trapped in one-, two-, or three-dimensional optical lattices. In the absence of a disordered potential, these systems feature two phases: superfluid (SF) and Mott insulator (MI). In the presence of a random disordered potential, a third insulating but compressible phase, known as Bose glass (BG), is stabilized [44]. As a result of finite disorder strength, no direct SF-MI phase transition exists, and the BG always intervenes between the MI and the SF regions according to the theory of inclusion [8].

3.2 Experimental realizations of disordered potential

In this section, I review several different experimental methods to create disordered potentials (both truly random disordered potential and quasi-periodic disordered potential) in the optical lattice. For example, disordered potentials can be realized by using speckle patterns, bichromatic lattices, introducing impurity atoms into the system, holographic techniques that produce point-like disorder, and so on. Here, I mainly focus on the first two methods: speckle patterns and bichromatic lattices.

3.2.1 Speckle patterns

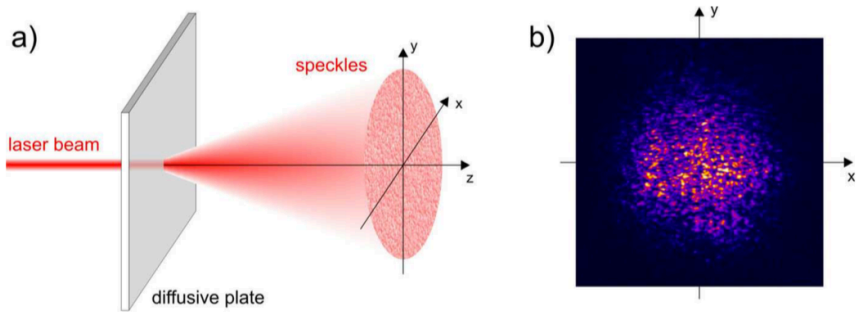

Figure 3.1: Production of speckle patterns. (a) A laser beam is passing through a diffusive plate to create the speckle pattens and the resulting speckle pattern is then imaged onto the atoms. (b) Intensity distribution of a typical speckle pattern recorded with a CCD camera. This figure is borrowed from Ref. [2].

Speckle pattern was the first method used to produce disordered potentials [72]. Speckle patterns are produced whenever the light is reflected by a device with a rough surface or light is transmitted through a diffusive medium. This kind of medium is called a diffusive plate. Figure 3.1(a) shows the experimental setup for producing the speckle pattern disordered potential by letting the laser beam

transmit through a diffusive plate. The diffusive plate is a plate made up of many random distributed impurities. After the laser beam is transmitted through the diffusive plate, a complex distribution of light is produced. Figure 3.1(b) shows the intensity distribution of a typical speckle pattern recorded with a CCD camera. This disordered distribution of light can be imaged onto the atoms, producing a disordered potential $V(\mathbf{r})$ proportional to the local laser intensity $I(\mathbf{r})$.

In general, as long as the wavelength of the light is far detuned from the atomic resonance and there is no absorption, the random disordered potential created by using speckle patterns is written as

$$V(\mathbf{r}) = \frac{3\pi c^2}{2\omega_0^3}\left(\frac{\Gamma}{\Delta}\right) I(\mathbf{r}) \quad , \tag{3.1}$$

where c is the speed of light, ω_0 is the frequency of the atomic resonance, Γ is the radiative linewidth, $\Delta = \omega - \omega_0$ is the detuning, and $I(\mathbf{r})$ is the density distribution. $V(\mathbf{r})$ is called density potential, and it is negative for the red detuning, $\Delta < 0$, and positive for the blue detuning, $\Delta > 0$. A negative $V(\mathbf{r})$ means atoms will move toward the higher intensity regions, while a positive $V(\mathbf{r})$ means atoms will move toward the lower intensity regions.

It needs to be noted that this kind of disordered potential is static, which means that for each experiment, it only realizes one disordered potential. But we can get another realization of disordered potential by shifting the position of the diffusive plate to change the pattern of disordered potential. Thus averages of multiple realizations of disordered potentials can be achieved in a simple way.

It also worth noting that the speckle pattern we discussed above is a two-dimensional pattern, where the pattern is in the plane perpendicular to the propagation axis. We can have a one-dimensional speckle pattern by using a cylindrical lens to stretch the pattern along one direction. A three-dimensional speckle pattern can be produced by adding another speckle pattern from a different direction.

3.2.2 Bichromatic lattice

The second common way to create disordered potentials is to use a bichromatic lattice. The bichromatic lattice is created in an experiment by using two laser beams to produce lattices with incommensurate wavelengths. The main laser beam with wavelength λ_1 is perturbed by a second laser beam with wavelength λ_2. By using these two optical lattices, a quasi-periodic disordered potential is produced. This kind of disordered potential is different from a truly random disordered potential or the disordered potential produced by speckle patterns, because the spectrum of the quasi-periodic disordered potential is made up of a set of discrete frequencies.

Figure 3.2 shows how to realize a bichromatic lattice. There are two kinds of laser beams with different wavelengths $\lambda_1 = 830$ nm and $\lambda_2 = 1076$ nm, where the first one can be seen as the main lattice and the second one can be seen as the disordering lattice. By adding those two lattices together, we can get the bichromatic lattice with the lattice potential:

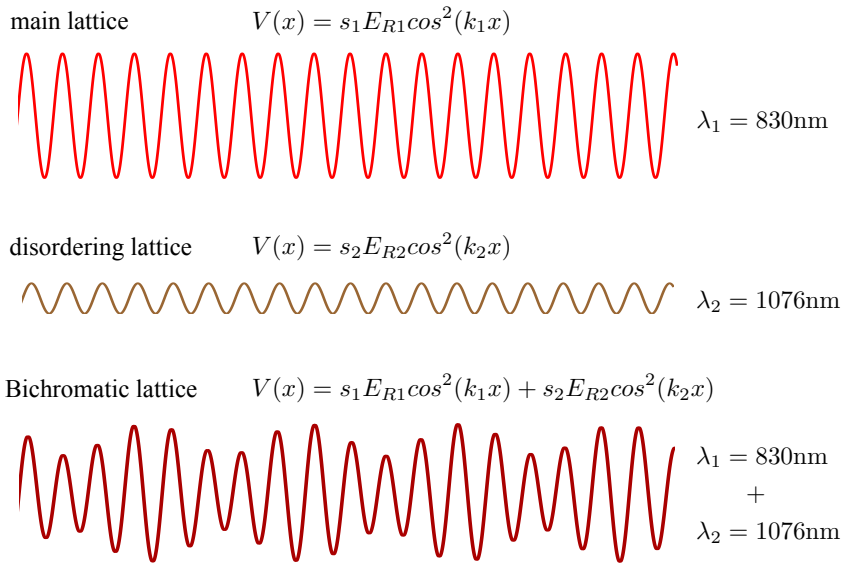

Figure 3.2: A bichromatic optical lattice. The discrete transitional invariance of the main lattice is perturbed by a secondary lattice with incommensurate wavelength. This figure is borrowed from Ref. [2].

$$V(x) = s_1 E_{R1} \cos^2(k_1 x) + s_2 E_{R2} \cos^2(k_2 x) \quad , \tag{3.2}$$

where $k_{1,2}$ is the lattice wavevector and E_{R1}=$\hbar^2\ k_1^2/2m$ and E_{R2}=$\hbar^2\ k_2^2/2m$ are the recoil energies. Here, the primary lattice height s_1 is much larger than the secondary lattice height s_2. Because $s_1 >> s_2$, the hopping amplitude J is determined by the main lattice height s_1. The effect of the first lattice can be seen as providing the hopping energy for the particles trapped in this optical lattice, while the effect of the second lattice is to induce a modulation of the on-site energies, which can be seen as a disordered potential.

3.2.3 Other methods

There are other ways to create disordered potentials. Here I explain two methods: introducing impurity atoms into the system [3] and holographic techniques which produce point-like disorder [4].

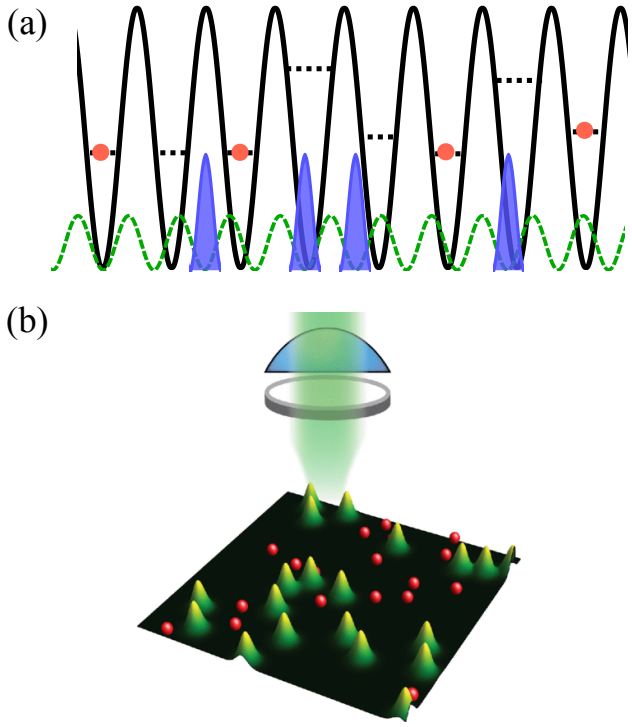

Figure 3.3: (a) To create a disordered impurity field, half the atoms of a lattice-trapped Bose gas are converted to an auxiliary spin state and localized to a state-selective incommensurate lattice (dashed green). (b) Schematic representation of the experimental implementation of the point-like disorder. These figures are borrowed from Ref. [3] and Ref. [4].

Figure 3.3(a) shows how to use atomic impurities to produce disordered potential in an optical lattice system. For this experiment setup, ^{87}Rb atoms are used to create a Bose-Einstein condensate. Initially, the system contains atoms in a certain hyperfine ground state. To create atomic impurities as shown in Figure 3.3(a), a fraction of the total population of atoms is transferred to

another spin state via a microwave sweep and is localized to a state-selective incommensurate lattice. Those atoms that are transferred to another spin state can be seen as atomic impurities in this optical lattice system. They act as point-like defects.

Figure 3.3(b) shows how to produce point-like disorder by using the holographic techniques in an experiment. First, ultracold atoms are confined in a quasi-two-dimensional geometry by using a sheet of far-detuned light. Then an additional laser beam is used to pass through a holographic disc to generate disordered potential. The disordered potential is focused on the atoms. The atoms experience a disordered potential consisting of a random arrangement of Gaussian barriers. The additional laser beam is represented by a green shaded region in Figure 3.3(b), and atoms are represented by red spheres.

3.3 Weakly interacting regime

The interplay between disordered potential and interaction has attracted much attention in the condensed matter field. Disordered potential always tends to localize particles. Different interactions lead to different phenomena. In the weakly interacting regime, repulsive interaction tends to delocalize particles, so the competition between disordered potential and repulsive interaction leads to a phase transition of the system from a localized state to an extended state (e.g., from an insulating phase to a superfluid phase). The situation is different in the strongly interacting regime. Strong interactions cooperate with disordered

potential and finally destroy the extended states, then the system is in a glassy or insulating phase. Here I provide a simplified picture of different interacting regimes for bosonic gas in the presence of disordered potentials, which is shown in Figure 3.4. Note that the real phase diagram is much more complicated.

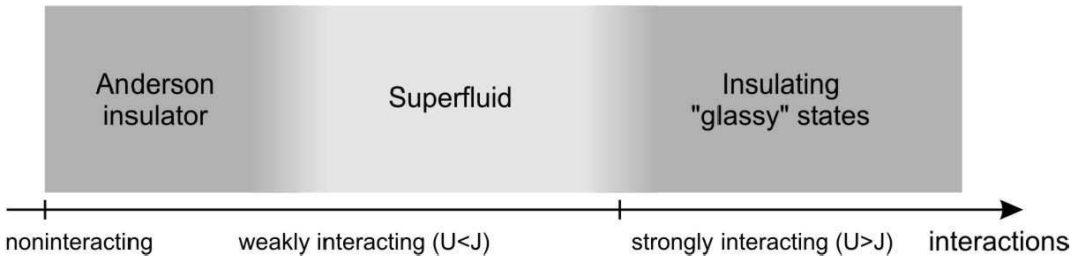

Figure 3.4: Pictorial representation of the different interaction regimes for a bosonic gas in the presence of disordered potentials. This figure is borrowed from Ref. [2].

3.3.1 Anderson localization

One of the interesting phenomena in random systems is Anderson localization. More than fifty years ago, Anderson showed that free fermions can be localized in the presence of random disordered potentials [9]. His idea can be described using a simple model of particles hopping on a lattice with random on-site energy. He found that when the on-site energy is above a critical disorder amplitude, the quantum states undergo a change from an extended state to a spatially localized state. The Hamiltonian of this simple model can be written as

$$H = -J\sum_j(\mid \omega_j\rangle\langle\omega_{j+1} \mid + \mid \omega_{j+1}\rangle\langle\omega_j \mid) + \sum_j \epsilon_j \mid \omega_j\rangle\langle\omega_j \mid \quad , \tag{3.3}$$

where the first term is the kinetic energy term or the hopping term with the hopping amplitude J, and the second term is the disordered potential term that contains on-site energies ϵ_j. ϵ_j is randomly distributed in the interval $[-\Delta, \Delta]$, Δ is the disorder strength, and $\mid \omega_j\rangle$ is the Wannier state localized at site j.

Anderson localized states are characterized by the typical exponential decay of the tails of their wavefunction in space distribution. For example, in the case of light, when we consider light traveling through a medium (like air, water, or sugar), since the medium is not perfect and contains some defects (defects can be seen as disorder), the light is scattered and can even be localized under some conditions [73]. This means the intensity of light decreases exponentially when it is traveling through a medium. For the quantum-mechanical wave functions, for large disorder, this means that a localized state $\Psi(x)$ can be written as

$$\Psi(x) \sim \exp(-\frac{x}{\xi}) \quad ,$$

where ξ is the localization length. Generally, the stronger the disorder, the smaller the localization length.

Whether the states are localized also depends on the dimensionality of the system. It is found that in one dimension, the states of these fermions are localized for any disorder strength; in two dimensions, the states are localized for any disorder strength, but the localization length at weak disorder can be exponentially large; in three dimensions, there exists a transition from the localized state to the extended state [9].

3.3.2 Experimental realization of Anderson localization: localization in a speckle disordered potential

Anderson localization of non-interacting bosons has been realized in experiments with both random disordered potentials and quasi-periodic potentials, by using speckle patterns or bichromatic lattices, respectively. In this section, I will present the results of an experimental study of the localization of particles in a Bose-Einstein condensate (BEC) in the presence of a disordered potential produced by speckle patterns [5]. In this experiment, first, a BEC is produced by using Rb atoms that are trapped in a magnetic trap. Then the condensate is transferred into a single beam optical dipole trap. After the system equilibrates to the ground state, the trapping laser beam is abruptly turned off, then the speckle pattern disordered potential is added to the BEC and the expansion of the BEC is observed.

Figure 3.5 shows the density profiles of the BEC. The top figure is the intensity profile of the speckle field used in the experiment. The bottom figure is the density profiles of the condensate after expansion in the disordered one-dimensional optical waveguide for different speckle height V_s; here, V_s is expressed in units of the BEC chemical potential $\mu = 2.5$ kHz in the initial trap. The bottom figure shows that when there is no speckle potential $V_s = 0$, the BEC expands freely. As the speckle potential heights V_s increase, both the expansion and the center of mass motion, which is induced by a small acceleration along the waveguide, start to be suppressed for $V_s \geq 0.25\mu$. The results of this experiment show that in the

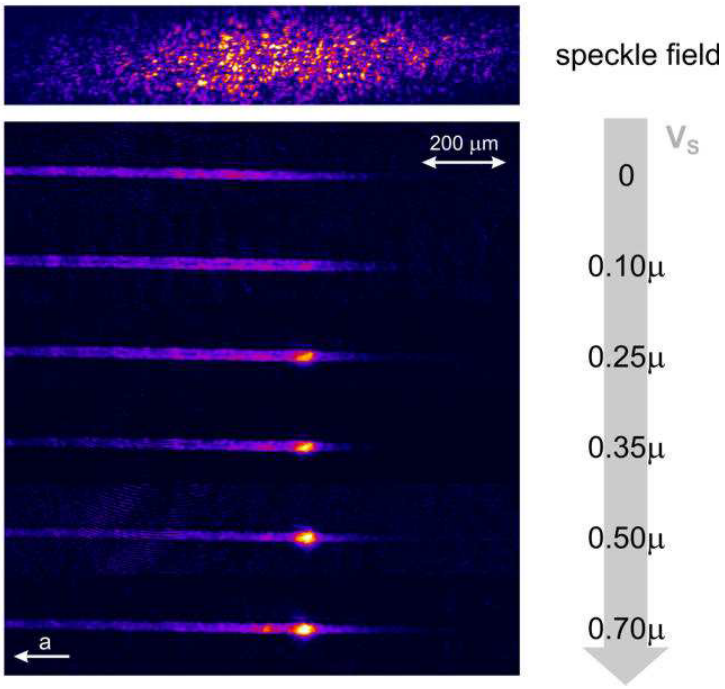

Figure 3.5: Expansion of a BEC in a disordered optical guide. The top figure is the intensity profile of the speckle field used in the experiment. The bottom figure shows the density profiles of the condensate after expansion in the disordered optical guide for different speckle heights V_s. This figure is borrowed from Ref. [5].

presence of the speckle pattern disordered potential, the one-dimensional BEC expansion is suppressed as the speckle height of the disordered potential increases.

A similar experiment has been done in Ref. [74], and the idea is the same: an initially trapped BEC of Rb atoms is left to expand freely in a one-dimensional waveguide in the presence of a speckle pattern disordered potential. The difference is that in Clement et al.'s paper [74], the waveguide is produced by a highly elongated magnetic trap, whereas in Fort et al.'s paper [5], the waveguide is produced by a single beam optical trap.

3.3.3 Experimental realization of Anderson localization: localization in a bichromatic lattice: Aubry-André model

In one dimension, a quasi-periodic disordered system displays a transition from extended to localized states, which is similar to Anderson localization. The difference is that in one dimension, in the presence of quasi-periodic disordered potential, the system undergoes the transition when the disordered strength is larger than the critical one, whereas in Anderson localization, the system in the presence of random disordered potential is always localized in one dimension no matter what the disorder strength is. This system with quasi-periodic disordered potential can be described by the Aubry-André model. The Hamiltonian of the Aubry-André model is

$$H = -J\sum_{j}(\mid \omega_j\rangle\langle\omega_{j+1} \mid + \mid \omega_{j+1}\rangle\langle\omega_j \mid) + \Delta\sum_{j}\cos(2\pi j\nu+\phi) \mid \omega_j\rangle\langle\omega_j \mid \quad , \quad (3.4)$$

where J is the hopping amplitude of the nearest neighbor sites, Δ is the disorder amplitude of the quasi-periodic modulations of the potential energy, ν is an irrational number, ϕ is a phase, and $\mid \omega_j\rangle$ is the Wannier state localized at site j.

The Hamiltonian in Equation 3.4 can also be rewritten as

$$H = -J\sum_{\langle i,j\rangle}({a_i}^{\dagger}a_j + h.c.) + \sum_{i} n_i\Delta\cos(2\pi i\nu + \phi) \quad , \quad (3.5)$$

where $\langle i,j\rangle$ denotes the sum over the nearest neighbor sites, $a_i^{\dagger}$ and a are the bosonic creation and annihilation operators at site i, and $n_i = a_i^{\dagger}a_i$ is the density

operator. In this model, the hopping term J tends to delocalize bosons, while the quasi-periodic disordered potential term Δ tends to localize bosons. This model can be solved analytically. Aubry and Audré analytically proved that this system undergoes a transition from extended to localized states at $\Delta = 2$. All states are extended for $\Delta < 2$, critical for $\Delta = 2$, and exponentially localized for $\Delta > 2$, with the same localization length $1/\ln(\Delta/2)$.

The experimental realization of Anderson localization of a non-interacting Bose-Einstein condensate (BEC) in the presence of quasi-periodic potentials was done by Roati et al. [6]. First, a cloud of interacting ^{39}K atoms is cooled in an optical trap to form a BEC, then the s-wave scattering length is tuned to almost zero using Feshbach resonances. The spatial size of the condensate can be controlled by changing the harmonic confinement provided by the trap. The quasi-periodic potential is imposed by using two laser beams in a standing-wave configuration. The main laser beam can be seen as the one that provides the hopping energy J, while the second laser beam provides the quasi-periodic disordered potential Δ. By abruptly switching off the main harmonic confinement and letting the atoms expand along the one-dimensional bichromatic lattice, the transport properties as well as the spatial and momentum distribution are investigated.

Figure 3.6(a) shows the detection of the spatial distribution of the atoms at increasing evolution times using absorption imaging. When $\Delta/J = 0$, the system expands ballistically, while in the limit of large disorder $\Delta/J > 7$, there is no diffusion. In-between those two values, a ballistic expansion with reduced speed is observed. Figure 3.6(b) shows the width of the atomic distribution versus the

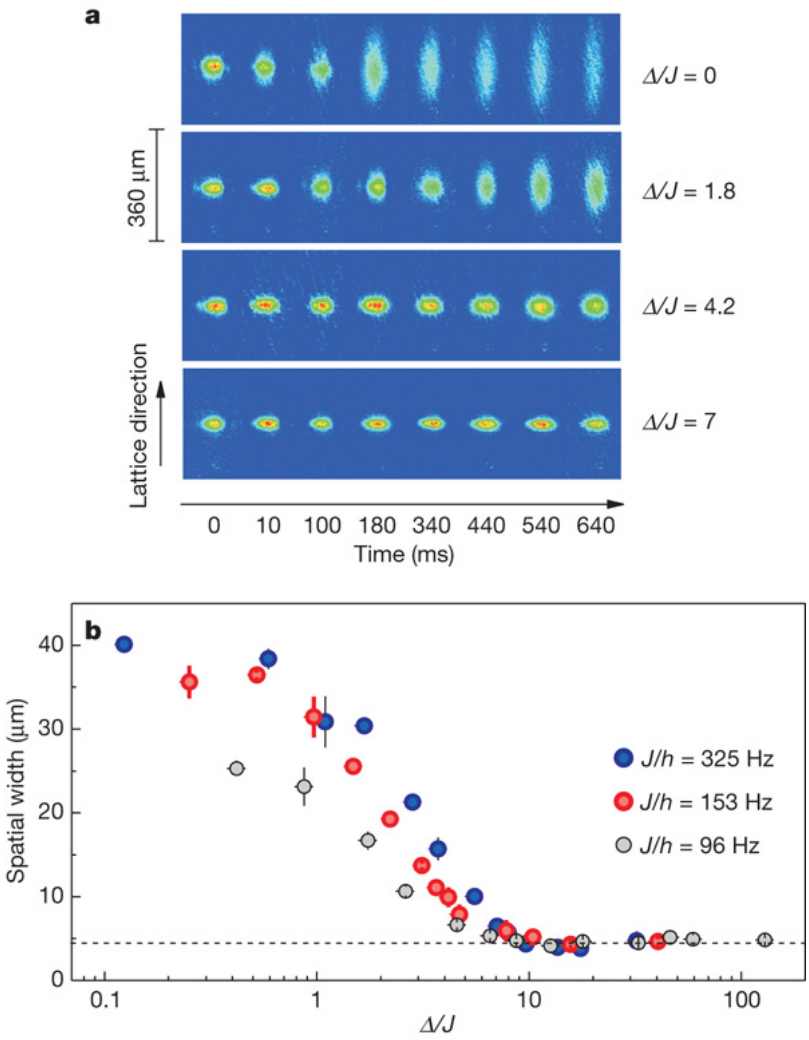

Figure 3.6: Probing the localization with transport. a) In-situ absorption images of the BEC diffusing along the quasi-periodic lattice for different values of Δ and $J/h = 153$ Hz. b) Rms size of the condensate for three different values of J, at a fixed diffusion time of τ =750 ms, vs. the rescaled disorder strength Δ/J. The dashed line indicates the initial size of the condensate. This figure is borrowed from Ref. [6].

rescaled disorder strength Δ/J, for three different values of J for a fixed evolution time of 750 ms. In all three cases, the system enters the localized regime at the same disorder strength, which agrees with the prediction of the Aubry-André model, that all the states are localized when $\Delta > 2$.

3.4 Strongly interacting regime

In the strongly interacting regime, we cannot ignore interactions among particles. This is much more reliable, because in nature, interactions among particles cannot be eliminated. We have discussed bosons in optical lattices with on-site interactions in Chapter 2, described by the Bose-Hubbard model. In the following, we consider interacting bosons in the presence of random disordered potentials.

3.4.1 Bose-Hubbard model with random disordered potential

In the presence of random disordered potential, the Hamiltonian is written

$$H = -J \sum_{\langle i,j \rangle} {a_i}^\dagger a_j + \frac{U}{2} \sum_i n_i(n_i - 1) - \sum_i \epsilon_i n_i \quad , \tag{3.6}$$

where a_i is the annihilation operator, $a_i^\dagger$ is the creation operator, and $n_i = a_i^\dagger a_i$ is the number operator. $\langle i, j \rangle$ denotes the sum over the nearest neighbor sites. J is the hopping amplitude, and U represents the on-site repulsive interaction energy. The disordered potential term ϵ_i has the range of $[-\Delta, \Delta]$, and it is the site-dependent energy.

The kinetic energy term tends to delocalize particles and reduce phase fluctua-

tions. The disordered potential term tends to localize particles. The combination of the interaction term and the random potential term tends to localize particles and reduce the density fluctuations. At zero temperature and integer filling factor, whether the system is in the superfluid phase or the insulating phase depends on the competition between kinetic energy and the combination of interactions and the random potential.

The phase diagram for the above system contains three phases. Along with the superfluid (SF) phase and the Mott insulator (MI) phase, there exists a third Bose glass (BG) phase. The BG phase is gapless and has finite compressibility, but it is still an insulating phase because of the localization effects of the random disordered potential. Many groups have investigated these random disordered potential cases, and they found that the BG phase must intervene between the MI and SF phases. If the random disorder strength is sufficiently strong, the MI phase can be completely destroyed.

In Fisher's paper [44], the zero temperature phase diagrams for the above system in μ/U vs. J/U plane are shown in Figures 3.7(a) and (b), depending on the competition between the disorder strength Δ and the on-site repulsive interaction U. The shape of the phase diagram is determined by the competition between the hopping term J, the on-site repulsive interaction term U, and the on-site disorder term Δ. Figure 3.7(a) shows that when disorder strength $\Delta < U$, the region of the MI phase has shrunk compared to the phase diagram without the disordered potential, which is shown in Figure 2.4 in Chapter 2.2. The MI phase is separated from the SF phase. There, the BG phase is intervened between

the SF and the MI phase. When the disordered potential Δ increases, the MI phase will continue to shrink and finally disappear when $\Delta > U$, which is shown in Figure 3.7(b).

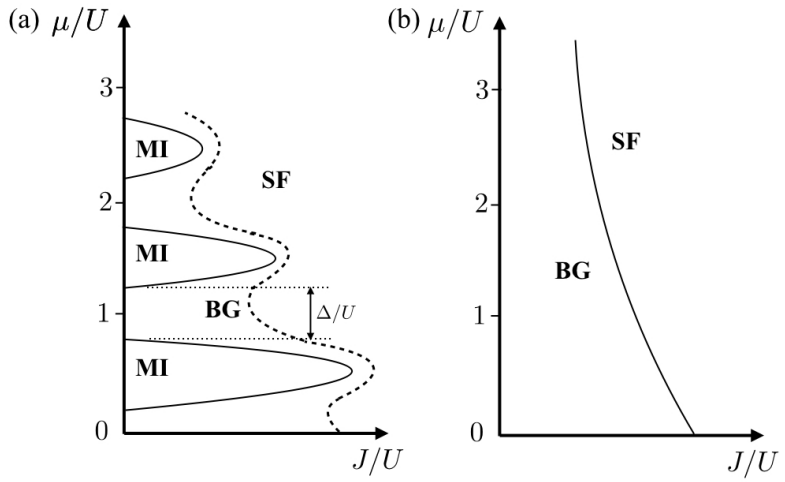

Figure 3.7: Zero-temperature phase diagram for the lattice model of interacting bosons, in the presence of disorder. Besides the superfluid phase and the Mott insulator phase, there exists the Bose glass phase: (a) represents the case where $\Delta < U$, and (b) represents the case where $\Delta > U$.

3.4.2 Phase diagram of the disordered Bose-Hubbard model in 3D

There have been many studies about the disordered Bose-Hubbard model in past decades using the mean field theory, density matrix renormalization group, and Monte Carlo method [57, 46, 45, 70, 8, 7, 47, 50, 71, 48]. The phase diagram of the disordered Bose-Hubbard model has been found in one, two, and three dimensions by using the quantum Monte Carlo method. Here I present the result in three dimensions.

The Hamiltonian of the Bose-Hubbard model in the presence of the random

on-site disordered potential is written in Equation 3.6. The phase diagram of the above system at filling factor $n = 1$ in three dimensions is shown in Figure 3.8. The x-axis is U/J and the y-axis is Δ/J. There are three phases inside: the superfluid phase (SF), the Mott insular phase (MI), and the Bose glass phase (BG). The critical transition points between the SF and BG phases are determined by scaling superfluid density ρ_s (see below), and the phase boundary has a "figure tip" at $60 \leq U/J \leq 120$. Reentrance behavior of the SF phase is also clear in this phase diagram. The BG phase is intervened between the SF and MI phases, and it is proved by the theory of inclusion [8].

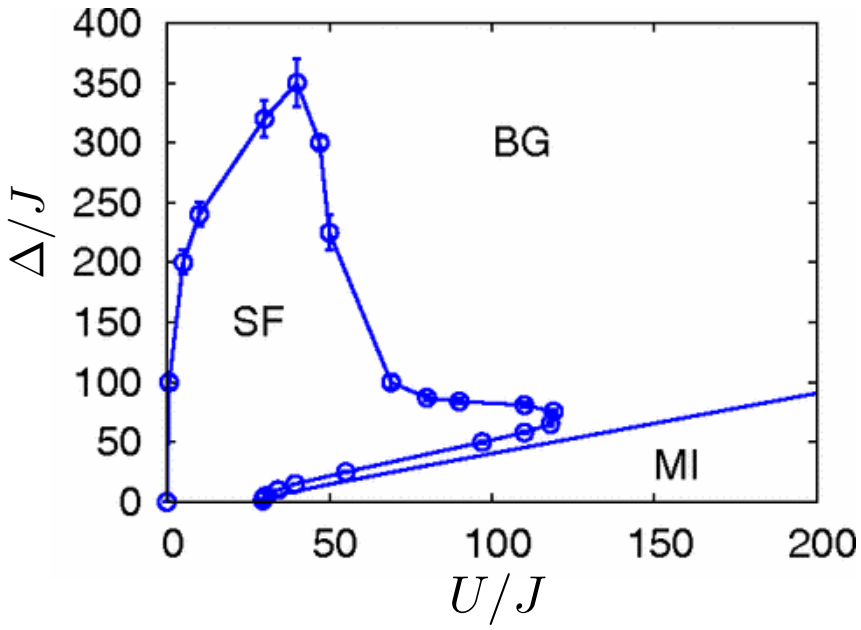

Figure 3.8: Phase diagram of the disordered 3D Bose-Hubbard model at filling factor $n = 1$, obtained by scaling the superfluid density ρ_s. This figure is borrowed from Ref. [7].

The phase boundary between the SF and BG phases is determined by scaling

the superfluid density ρ_s [8]. The superfluid density ρ_s is related to the winding number, where $\rho_s = \langle \mathbf{W}^2 \rangle / dL^{d-2}\beta$ [75], $\mathbf{W}$ is the winding number in space, d is the spatial dimension ($d = 3$ in this case), L is the system size, and $\beta = 1/T$ is the inverse temperature. A typical finite size scaling method is shown in Figure 3.9. Here, the author plot the interaction strength U/J as a function of winding number square $\langle \mathbf{W}^2 \rangle / 3$ for different system sizes $L = 4$, 8, 16, 24, and 32. The dynamical critical exponent is chosen to be $z = 2$ for numerical convenience, where a repeated calculation with $z = 1$ gives the same critical point. By using consecutive crossing points determined by the main plot in Figure 3.9, the critical transition point is extracted by plotting $(U/J)_c$ as a function of $(1/L)^2$. The inset in Figure 3.9 shows the extrapolation of the intersection points $(U/J)_c$ as a function of $(1/L)^2$. The transition point is $(U/J)_c = 30.57$.

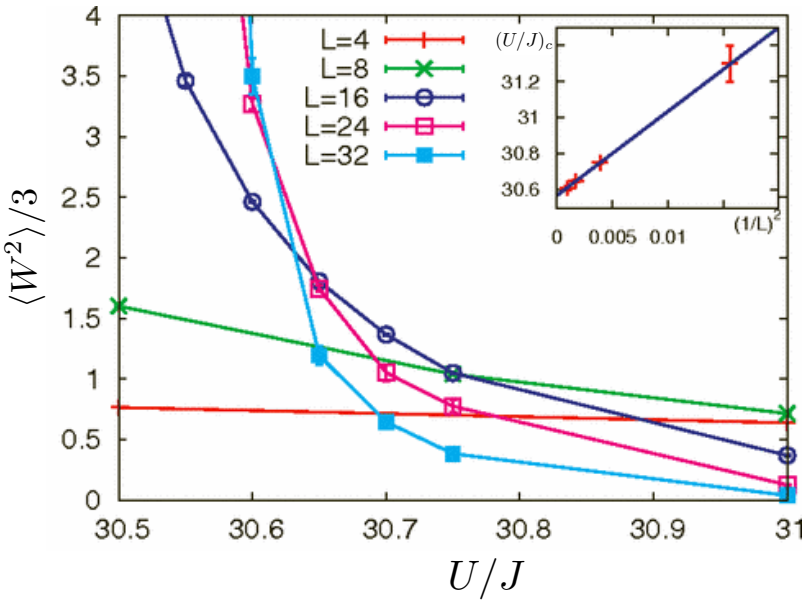

Figure 3.9: Finite size scaling analysis for the winding number fluctuations for $\Delta/J = 5$ using the dynamical exponent $z = 2$. The inset shows the extrapolation of the intersection points with a $(1/L)^2$ law yielding $(U/J)_c = 30.57$. This figure is borrowed from Ref. [8].

Chapter 4

Path integral Monte Carlo and the Worm algorithm

Quantum Monte Carlo is one of the most powerful methods to study the equilibrium properties of strongly interacting many-body systems. While there are many different Monte Carlo methods (i.e., stochastic series expansion, diffusion Monte Carlo, variational Monte Carlo, path integral Monte Carlo), I am using the path integral Monte Carlo method, implemented by the Worm algorithm [76, 77]. In this chapter, I will introduce path integral Monte Carlo method with the Worm algorithm.

4.1 Path integral Monte Carlo

Let us consider a system with Hamiltonian $H = H_0 + H_1$, where H_0 is diagonal in a basis set $\{|\alpha\rangle\}$ and H_1 is nondiagonal. The partition function, which describes the equilibrium properties of the system, is defined as the trace of the density matrix operator. In the interaction picture, the partition function is written as:

$$Z = \mathrm{Tr}[e^{-\beta(H_0+H_1)}] = \mathrm{Tr}[e^{-\beta H_0}\mathrm{T}_\tau e^{-\int_0^\beta H_1(\tau)d\tau}] \quad , \tag{4.1}$$

where Tr is the trace of an operator, $\beta = 1/T$ is the inverse temperature with $k_B = 1$, T_τ is the "time" ordering operator, $\tau = it$ is the imaginary time, and $H_1(\tau) = e^{\tau H_0} H_1 e^{-\tau H_0}$. Here $H_1(\tau)$ is H_1 expressed in the interaction picture.

By using Feynman path integral formulation, the partition function can be rewritten as follows:

$$Z = \sum_{\{|\alpha\rangle\}} \langle\alpha| e^{-E_\alpha \beta} \Big(1 - \int_0^\beta d\tau H_1(\tau) + (-1)^m \int_0^\beta d\tau_m \cdots \int_0^{\tau_2} d\tau_1 H_1(\tau_m) \cdots H_1(\tau_1) + \cdots \Big) |\alpha\rangle \quad , \tag{4.2}$$

where E_α are eigenvalues of H_0 and the integrals are time ordered. The summation over states $\{|\alpha\rangle\}$ comes from the trace.

Next we insert the completeness relation $\sum_{\alpha'} |\alpha'\rangle\langle\alpha'|$ between $H_1(\tau_i)$. To make things simple, before integration over time, we write down only the mth term:

$$(-1)^m d^m\tau e^{-(\beta-\tau_1)H_0^{\alpha_0}} \big(H_1^{\alpha_0,\alpha_1}\big) e^{-(\tau_1-\tau_2)H_0^{\alpha_1}} \cdots \big(H_1^{\alpha_{m-1},\alpha_m}\big) e^{-\tau_m H_0^{\alpha_m}} \quad , \tag{4.3}$$

where $d^m\tau = d\tau_1 \cdots d\tau_m$. Considering the trace condition (i.e., a periodic boundary condition in imaginary time), we have $\alpha_m = \alpha_0$.

Below, I explain how the path integral Monte Carlo method works on the Bose-Hubbard model. The Hamiltonian of the Bose-Hubbard model can be rewritten in two terms:

$$H = -J \sum_{\langle i,j \rangle} {a_i}^\dagger a_j + \frac{U}{2} \sum_i n_i(n_i - 1) - \sum_i \mu_i n_i = H_1 + H_0 \quad . \tag{4.4}$$

Here we choose the Fock basis. The Fock basis is represented by $|\alpha\rangle = |\{n_i\}\rangle =$

$|n_1 \cdots n_i \cdots n_N\rangle$, where n_i is the occupation number on site i and N is the total number of sites. In the Fock basis, the on-site interaction term and chemical potential term are diagonal and the hopping term is nondiagonal.

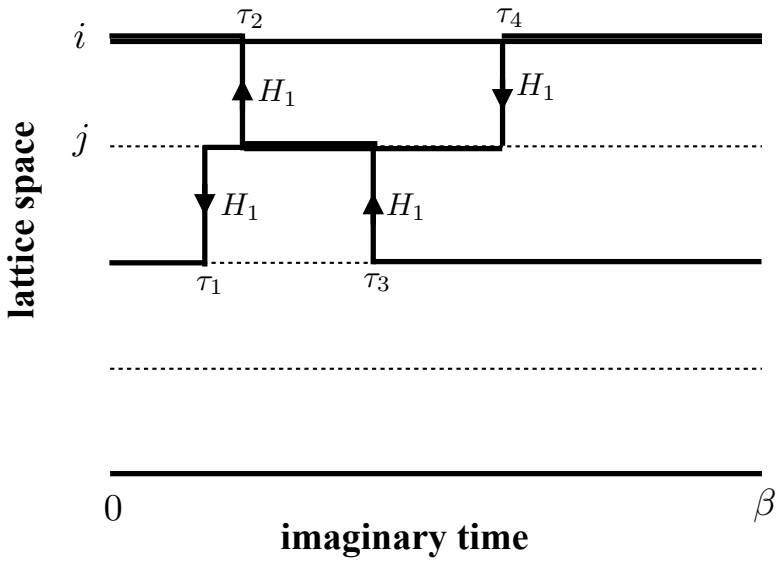

Figure 4.1: Sketch of lattice path integral representations for the partition function. Line thickness is proportional to n_i. The points in imaginary time where the system changes state are called "kinks".

The hopping term H_1 changes the state by shifting only one particle to a nearest neighbor site. The sequence of matrix elements in Equation 4.3 is determined by specifying the imaginary time trajectory of occupation numbers $\{n_i(\tau)\}$. Expression of the hopping elements in Equation 4.3 is written as $H_1^{i,j} = \langle n_i + 1, n_j - 1| - Ja_i^\dagger a_j |n_i, n_j\rangle = -J\sqrt{(n_i+1)n_j}$. The potential term H_0 is diagonal in the Fock basis. We use $H_0(\tau)$ as the energy of the state $|\{n_i(\tau)\}\rangle$. Figure 4.1 is a diagram associated with one of the fourth order terms (here $m = 4$) which contributes $J^4 d\tau_1 d\tau_2 d\tau_3 d\tau_4 1 \cdot 2 \cdot \sqrt{2} \cdot \sqrt{2} \exp\{-\int_0^\beta d\tau H_0(\tau)\}$ to the partition

function. Each line represents a particle and it is called "worldline". The points in imaginary time where the system changes state are called "kinks".

Thus one can rewrite partition function in Equation 4.2 as a sum over all configurations such that $n_i(\beta) = n_i(0)$:

$$Z = \sum_{\{n_i(\tau)\}} W[\{n_i(\tau)\}] \quad , \tag{4.5}$$

where $W[\{n_i(\tau)\}]$ is the weight of each configuration. A configuration can be pictorially represented as in Figure 4.1. Because the partition function is a trace, the periodic boundary condition in imaginary time has to be satisfied. As a result, the configuration shown in Figure 4.1 can be wrapped on a torus. We call these configurations the Z configuration space.

4.2 The Worm algorithm

The Worm algorithm works in an enlarged configuration space [76, 77, 78]. It changes the configuration by allowing one disconnected worldline. This disconnected worldline is known as the "worm". The configuration space with the worm is called the G configuration space because, in this enlarged configuration space, one can efficiently collect statistics for the Green function.

The Green function of the system is given by

$$G(\tau_M - \tau_I, i_M - i_I) = T_\tau \langle a^\dagger_{i_M}(\tau_M) a_{i_I}(\tau_I) \rangle \quad . \tag{4.6}$$

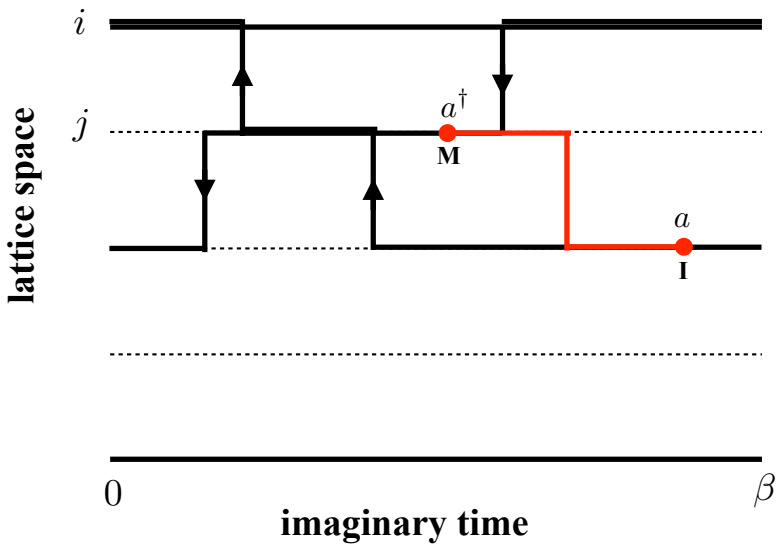

Figure 4.2: Sketch of lattice path integral representations for the Green function. Line thickness is proportional to n_i. Operator $a^\dagger$ is the bosonic creation operator, and a is the bosonic annihilation operator. Those two end points are labeled I (*Ira*) and M (*Masha*).

Figure 4.2 shows the lattice path integral representations for the Green function. It looks similar to Figure 4.1 with one difference: due to operator $a^\dagger$ at point (i_M, τ_M) and a at point (i_I, τ_I), we have one disconnected worldline present in the system on the time interval (τ_I, τ_M). Here τ represents imaginary time. Those two end points in Figure 4.2 are labeled I (*Ira*) and M (*Masha*).

Regarding updates, we only describe updates performed with the $Masha$-end of the open worldline. The updates performed with the Ira-end follow from time reversal symmetry. There are four types of updates: *open/close*, *insert/remove*, *move*, and *jump/anti-jump* [78].

Open/Close: This pair of updates changes the configuration back and forth between the Z space and G space. The *open* update changes the configuration

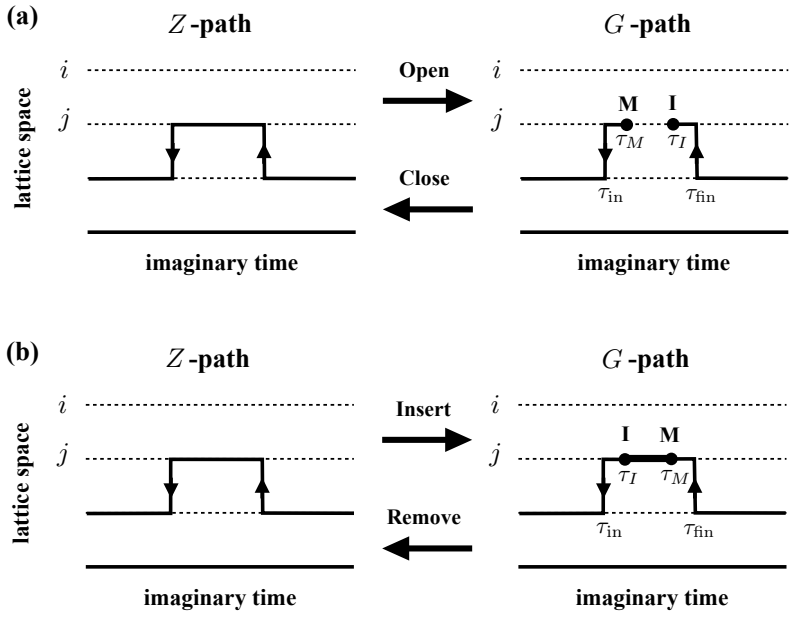

Figure 4.3: (a) Transformations performed by the *open/close* pair of updates. (b) Transformations performed by the *insert/remove* pair of updates.

by selecting an existing worldline and erasing a small part of the worldline. The *close* update does the opposite by selecting an existing worldline and drawing a small piece of worldline between the end points (M and I) of the open line to complete the loop. Figure 4.3(a) shows the *open/close* updates.

Insert/Remove: This pair of updates also switches the configuration back and forth between the Z space and G space. The *insert* update changes the configuration by drawing a small part of the worldline between the end points. The *remove* update does the opposite by erasing a small piece of worldline between the end points. These two updates are similar to the *open/close* updates except that the time ordering of τ_I and τ_M is reversed. Figure 4.3(b) shows the *insert/remove* update.

Move: This update works in the G space. It moves $Masha$ from τ_M to τ'_M.

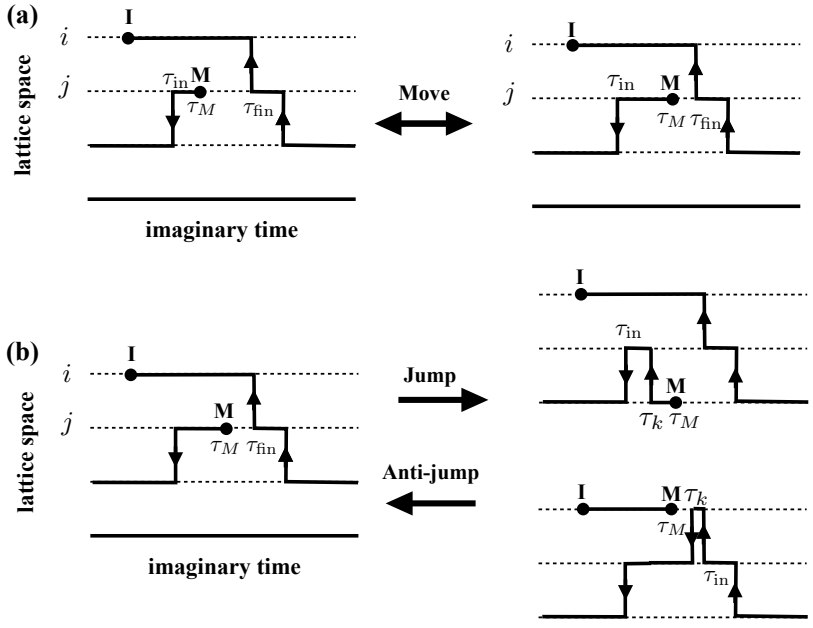

Figure 4.4: (a) Transformations performed by the *move* update. (b) Transformations performed by the *jump/anti-jump* pair of updates.

This moving motion is equivalent to drawing or erasing a piece of the worldline. Figure 4.4(a) shows the *move* update.

Jump/Anti-jump: This pair of updates are different from all above updates. Instead of changing the time position of $Masha$, these two updates change the motion of the end points in space. The points in imaginary time where the system changes state are the "kinks". We place $Masha$ on the neighboring site and connect worldlines of the two sites involved in the update in such a way that the rest of the path remains intact. There is one difference between these two updates. When the kink is inserted to the left of $Masha$ (*jump* update), we can still see it as drawing the same worldline. However, when the kink is inserted to the right of $Masha$ (*anti-jump* update), we can see it as reconnecting the existing worldlines. Figure 4.4(b) shows the *jump/anti-jump* updates.

In conclusion, the updates described above allow us to draw or erase any line and jump between lines. The Worm algorithm works in an enlarged configuration space by introducing disconnected loops. This results in working in the grand-canonical ensemble, where particles can be added to or removed from the system. The Worm algorithm is based on local updates but can efficiently sample configurations that are topologically different (e.g., configurations with different winding numbers). Figure 4.5 shows two topologically distinct configurations with 0 and 1 winding numbers. The superfluid density ρ_s can be extracted from the winding numbers [75]:

$$\rho_s = \frac{\langle \mathbf{W}^2 \rangle}{dL^{d-2}\beta} \quad , \tag{4.7}$$

where β is the inverse temperature, L is the system size, d is the dimensionality, and $\mathbf{W}^2 = \sum_{i=1}^{d} W_i^2$.

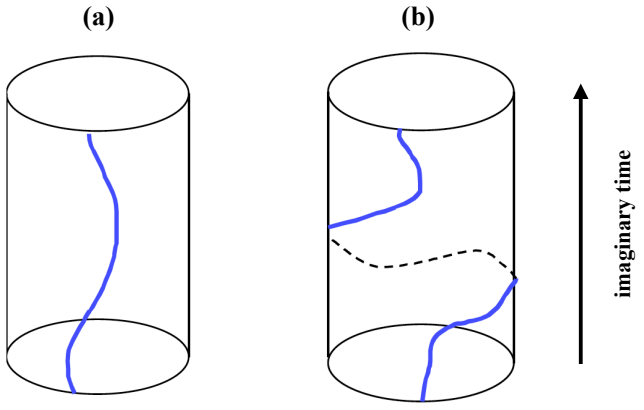

Figure 4.5: Two configurations with 0 (a), and 1 (b) winding numbers.

4.3 Example

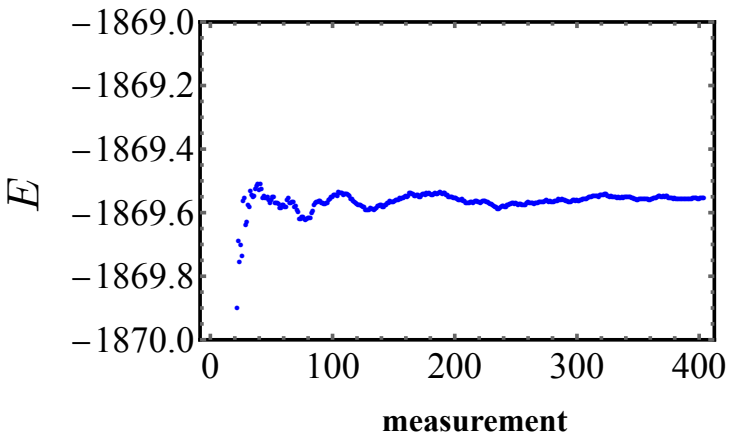

Figure 4.6: Energy E as a function of measurements in a thermalized situation.

In the following, I use an example to show how to calculate the error of the energy E. Figure 4.6 shows the energy E as a function of measurements for the Hamiltonian in Equation 5.1 with system size $L = 21$, on-site interaction $U/J = 2$, and disorder strength $\Delta/J = 20$. Each data point is the average value of E over all the previous measurements. The measurements are made every certain number of MC steps so that configurations are independent. The choice of the number of MC steps between two measurements is adjusted according to the parameters of the model (e.g., the Hamiltonian of the system, the inverse temperature β, the system size L) to make sure it is larger than the autocorrelation time. In practice, the number of MC steps between two measurements is chosen to be much larger than the degree of freedom of the system.

As shown in Figure 4.6, the energy E fluctuates during the first 200 measurements and then tends to be flat, indicating the system is thermalized. Thermal-

ization means the simulated configurations come from a small but representative configuration space [79]. Sampling a small but representative configuration space is the concept of *important sampling*. This is because the number of configurations is extremely large; but in many cases, only a small fraction of configurations is needed in order to get a reliable estimate of the physical observable, such as, the energy E.

Starting MC simulations from arbitrary configurations we are unlikely to hit this small but representative configuration space. Sometimes it takes a long time for the algorithm to walk its way to the representative configuration space. In this situation, the energy still fluctuates after a large number of measurements. The fluctuation of the physical observables after a large number of measurements happens in different scenarios. For example in disordered systems, close to a transition point, the system needs more time to thermalize.

Once we get the measurements of E as shown in Figure 4.6, we throw away the first several hundred measurements that are not thermalized. Then the value of E is the mean value of the thermalized measurements, and the error of E comes from the standard deviation of the thermalized measurements.

Chapter 5

Equilibrium phases of two-dimensional bosons in quasi-periodic lattices

5.1 Introduction

In this chapter, I present numerical results of bosons in a two-dimensional square lattice in the presence of a quasi-periodic disordered potential. The material presented in this chapter is based on my work published in Ref. [49]. Quasi-periodic disordered potential can be realized using a bichromatic lattice which has been described in Chapter 3.2.2. Here, I use path integral quantum Monte Carlo by the Worm algorithm [76] to study ground state phase diagram of the above system. The same system in the quasi-periodic disordered potential in one-dimension has been studied using the density matrix renormalization group. Similarly to what was observed in one dimension [80], I find that if the interaction strength is smaller than the critical interaction strength corresponding to the two-dimensional superfluid to Mott insulator (SF-MI) transition in the clean system, sizable disorder is needed to destroy superfluidity. On the other hand, at any given disorder, one can find an interaction strength above which superfluidity is completely destroyed in favor of an insulating phase. At lower disorder strength this insulating phase is a Mott insulator (MI), while at larger disorder strength it is a Bose glass (BG). The numerical results for the compressibility in the range of interaction strengths where SF has completely disappeared are consistent with

a direct MI-BG phase transition and do not show any evidence of a crossover region characterized by Mott-glass-like (MG) behavior (or anomalous Bose glass), unlike the findings of [81] for the case of random disorder. Finally, at intermediate interaction strengths, the system undergoes an insulator to superfluid transition upon increasing the strength of the disorder. The system (re)enters the Bose glass phase by further increasing of disorder strength.

5.2 System Hamiltonian

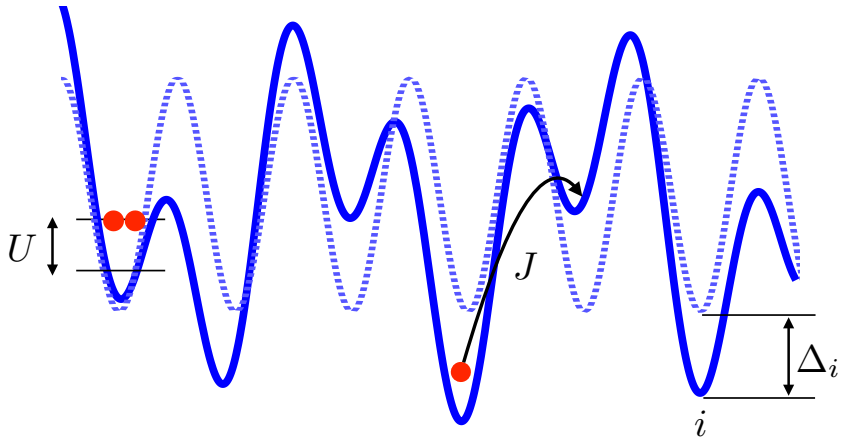

Figure 5.1: Schematic representation of bosonic lattice system in 1D. The blue dotted line represents the original optical lattice without the disordered potential. The blue solid line represents the quasi-periodic optical lattice. The red circles are bosons.

In this section, I study a system of bosons in a two-dimensional square lattice in the presence of quasi-periodic disordered potential, described by the Hamiltonian:

$$H = -J \sum_{\langle i\, j \rangle} (a_i^\dagger a_j + h.c) + \frac{U}{2} \sum_i n_i(n_i - 1)$$
$$- \mu \sum_i n_i + \sum_i \Delta_i n_i \quad . \tag{5.1}$$

The first term in the Hamiltonian is the kinetic energy, where $a_i^\dagger$ (a_i) are the bosonic creation (annihilation) operators with the usual commutation relations, and J is the hopping matrix element between sites i and j. I use $\langle \cdots \rangle$ to denote nearest neighboring sites. Here, U sets the strength of the on-site repulsion and μ is the chemical potential, which in the absence of disorder, sets the number of particles in the system. The quasi-periodic on-site disorder Δ_i is created by perturbing the primary optical lattice with a second incommensurate one. The net result is a quasi-periodic external potential that couples to the on-site density n_i. Hence, the on-site disorder takes the form $\Delta_i = \Delta \cos(2\pi\beta_d x_i + \phi_x) \cos(2\pi\beta_d y_i + \phi_y)$, where Δ is the strength of disorder, $\phi_{x,y}$ is an arbitrary phase shift, and β_d measures the degree of commensurability. Both Δ and β_d can be tuned experimentally, the former by tuning the relative heights of the primary and secondary lattices and the latter by varying the wave numbers of the two lattice potentials. The results presented below correspond to the maximally incommensurate ratio given by the choice $\beta_d = (\sqrt{5} - 1)/2$.

Figure 5.1 is the schematic representation of bosonic lattice system in one dimension. The blue dotted line represents the original optical lattice without the disordered potential. The blue solid line represents the quasi-periodic optical lattice. The red circles are bosons. J characterizes the hopping amplitude, U characterizes the on-site repulsive interaction, and Δ_i characterizes the quasi-periodic disordered potential on site i.

5.3 Ground state phase diagram

In the following, I present a numerical study of the Hamiltonian in Equation 5.1 at unit filling ($n = N/N_{\text{sites}} = 1$) by means of quantum Monte Carlo simulations using the Worm algorithm. In order to obtain accurate results in the thermodynamic limit I perform finite-size scaling on the simulation results. This process is challenging in the presence of quasi-periodic disorder where the disorder is incommensurate with the lattice. Incommensurability means that one cannot produce comparable systems by simply scaling the lattice size. To circumvent this problem I have used system sizes L, with $N_{\text{site}} = L \times L$, from the Fibonacci sequence [82]. Unlike the results reported for one-dimensional systems [82], I have found that for disorder strength $\Delta \gtrsim 3J$, our results depend strongly on the choice of (ϕ_x, ϕ_y). Hence, for each set of parameters (μ, Δ, U, L), I have run simulations with fifty different choices for phases $\phi_{x,y} \in [0, 2\pi)$. The results presented below are extracted from the fifty runs using the bootstrap method. I find that further averaging over (ϕ_x, ϕ_y) realizations simply reduces the statistical error.

The ground state phase diagram of the system at unit filling is shown in Figure 5.2, where the horizontal and vertical axes correspond to U/J and Δ/J, respectively. At lower disorder strength and for $U/J \lesssim 16$ the system is in the superfluid state associated with the presence of off-diagonal long-range order. The superfluid phase is characterized by finite compressibility and non-zero single particle condensate order parameter, $\langle\psi\rangle = \langle a_i\rangle \neq 0$, associated with a finite superfluid stiffness ρ_s. The superfluid stiffness is extracted from simulations using

the relation $\rho_s = \langle \mathbf{W}^2 \rangle / dL^{d-2}\beta$, where $\mathbf{W}$ is the winding number in space, d is the spatial dimension ($d = 2$ in our case) [75], and $\beta = 1/T$ is the inverse temperature. In all our simulations I have chosen β such that the system is in its ground state, and have scaled $\beta \propto L^z$ where z is the dynamical critical exponent. The SF phase becomes unstable at stronger disorder strength and a transition to the insulating BG phase occurs. The BG phase is characterized by vanishing superfluid stiffness ρ_s and finite compressibility κ. The region of parameter space corresponding to $U/J \lesssim 10$ has not been explored extensively as finite size effects are much more pronounced. In this region finite size scaling becomes much more difficult resulting in large statistical errors.

For $16 \lesssim U/J \lesssim 35$ and at low disorder strength, the system is in an insulating phase and undergoes a phase transition in favor of the SF phase upon increasing the disorder strength. A similar phase transition is present if the trapping potential features random disorder, where it has been shown that the presence of an intervening BG phase between the MI and SF is guaranteed by the theorem of inclusions [8]. It should be noted that this theorem does not apply to quasi-periodic disorder and therefore the existence of the BG phase or the lack thereof should be confirmed by direct measurement of the compressibility. However, the parameter regime corresponding to the range of interactions and disorder strengths where the BG region may form is narrow. As for the case of random disorder, the compressibility of the BG in narrow regions would be too small to be detected numerically, making it impossible to distinguish between the MI and BG phases. I am therefore unable to discuss the onset of the BG phase, and generically refer to

the dashed blue region separating the SF and the zero-disorder MI in Figure 5.2 as an insulating phase. Further increasing the disorder strength results in the destruction of the SF order in favor of the BG.

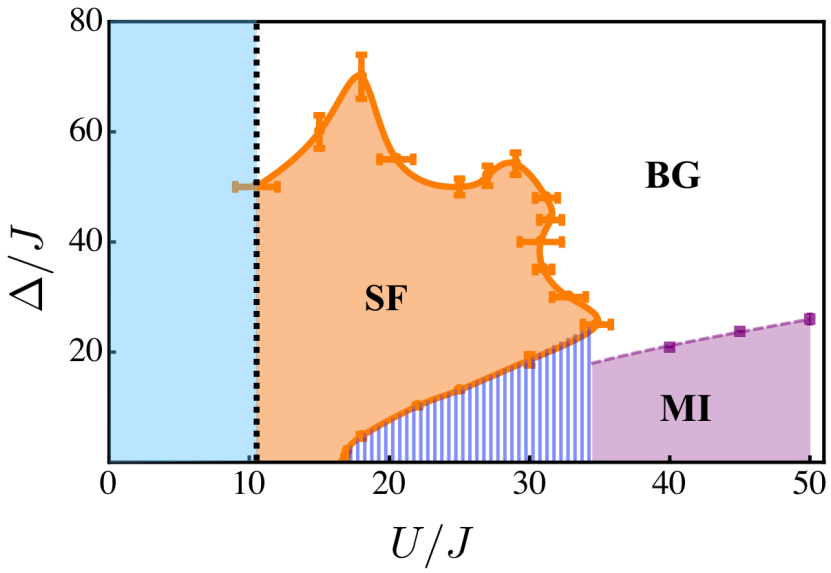

Figure 5.2: Ground state phase diagram of the system described by Equation 5.1 at filling factor $n = 1$. The horizontal and vertical axes are the on-site interaction strength U/J and disorder strength Δ/J, respectively. Using these two parameters as tuning knobs, the system can form a Mott-Insulator (MI), a superfluid (SF), and a Bose glass (BG). Simulations results for the SF-insulator phase boundary are shown using solid orange circles (the solid orange line is a guide to the eye), while solid purple squares (the dashed line is a guide to the eye) correspond to the phase boundary between the MI and BG phases. At lower disorder and intermediate interactions I am unable to distinguish between the MI and the BG (dashed blue region). Error bars are within the symbols if not shown in the figure.

Figure 5.3(a) illustrates the finite size scaling procedure used to determine the SF-BG (or generic insulator) phase boundary (solid orange circles in Figure 5.2). Here I plot the scaled superfluid stiffness $\rho_s L^{(d+z-2)}$ with $z = 2$, as a function of Δ/J at $U/J = 22$ and $L = 21$, 34, 55, and 89 (red circles, blue squares, empty black squares, and black diamonds, respectively). In these simulations, I have

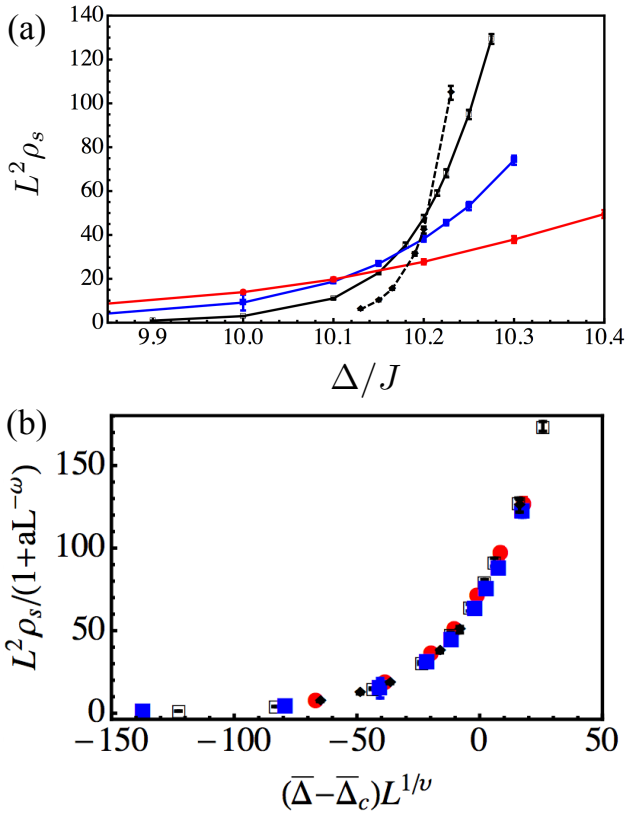

Figure 5.3: (a) Scaled superfluid stiffness $\rho_s L^{-(d+z-2)}$ with $z = 2$, as a function of Δ/J for $U/J = 22$ and $L = 21$, 34, 55, and 89 using red circles, blue squares, empty black squares, and black diamonds, respectively. In these simulations I have used $\beta = (L/2)^2$ to scale the imaginary time dimension L_τ. (b) Data collapse using $\nu = 0.67$, $a = -9.4$, $\omega = -0.9$, and $\bar{\Delta}_c = 10.21$ corresponding to the critical point extracted from the main plot. Here $\bar{\Delta} = \Delta/J$. The symbols are the same as those used for (a). Error bars are within the symbols if not shown in the figures.

used $\beta = (L/2)^z$ to scale the imaginary time dimension L_τ. The dynamical critical exponent z was set to $d = 2$, following the prediction in Ref. [44] for random disorder, and the recent unambiguous confirmation using Monte Carlo techniques [83]. The drift in the position of the intersection point indicates that a correction to the finite size scaling relation $\rho_s L^{(d+z-2)} = f(L^{1/\nu}\frac{\Delta}{J}, \beta L^{-z})$ where $f(x, \text{const})$ is a universal function, must be included in order to observe data collapse. After this correction is taken into account the scaling relation takes the form $\rho_s L^{(d+z-2)} = (1 + aL^{-\omega})\, f(L^{1/\nu}\frac{\Delta}{J}, \beta L^{-z})$ [84]. Figure 5.3(b) shows

$L^2\rho_s/\left(1+aL^{-\omega}\right)$ as a function of $(\bar{\Delta}-\bar{\Delta}_c)L^{1/\nu}$, where $\bar{\Delta}=\Delta/J$. From the best data collapse I find $\nu=0.67\pm0.07$ ($\nu=0.67$ holds for the SF-insulator transition of a clean system), $a=-9.4\pm0.5$, $\omega=-0.9\pm0.05$, and $\bar{\Delta}_c=10.21\pm0.05$. This value of ν suggests that the quasi-periodic disorder is still irrelevant for $\Delta/J\sim10$. As noted above, the choice of dynamical exponent $z=d$ has only been predicted and confirmed for random disorder. To ensure that our choice of the critical exponent z does not affect the position of the transition line, I have performed finite size scaling with a choice of $z=1.5$ for various points on the transition line. I find that the critical point remains the same within the error bars for the two different choices of z.

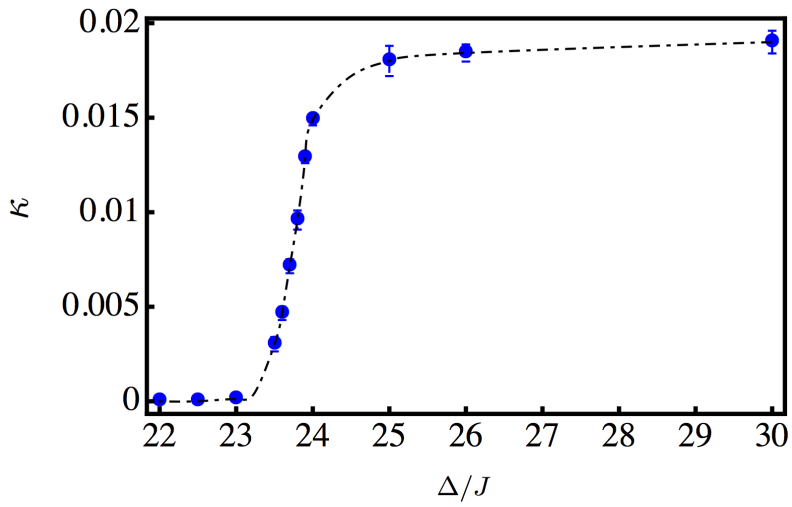

Figure 5.4: Compressibility κ vs. Δ/J for $U/J=45$, $L=21$, and $\beta=L/2$. The compressibility becomes finite at $\Delta/J\sim23.5$ and plateaus at $\Delta/J\sim24.5$. Error bars are within the symbols if not shown in the figure.

Finally, I turn the attention to the region $U/J\gtrsim35$ where the SF phase is completely absent and the system undergoes a MI-BG transition upon increasing the disorder strength. In this region of the parameter space I can easily measure

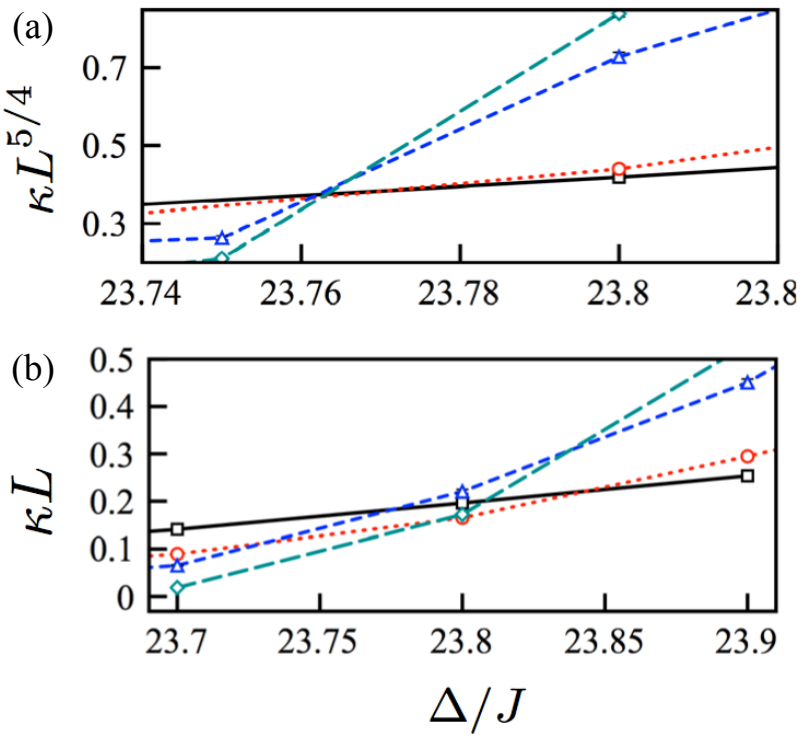

Figure 5.5: The top (a) and bottom (b) panels show κL^{d-z} versus Δ/J for $z = 0.75$ and $z = 1$, respectively, at $U/J = 45$. The scaled compressibility is shown for $L = 21$, 34, 55, and 89 using black squares, red circles, blue triangles, and green diamonds, respectively. The data indicates that $0.75 \lesssim z \lesssim 1.25$. Error bars are within the symbols if not shown in the figures.

compressibility and distinguish between the MI and BG phases. To this end I have performed simulations with z =0.75, 1, 1.25, and 1.5 at $U/J = 45$. Figure 5.5 shows the scaled compressibility κL^{d-z} with $z = 0.75$ (a) and $z = 1$ (b) for L =21, 34, 55, and 89 using black squares, red circles, blue triangles, and green diamonds, respectively. While I have not performed an exhaustive scan over different values of dynamical exponent z, I find that the best crossing corresponds to $z = 0.75$ and gives the critical point at $\Delta_c/J = 23.76 \pm 0.05$.

Lastly, I discuss the possibility of the existence of a crossover region separating the MI from the BG, where the system forms a Mott glass or possesses a Mott-

glass-like anomalous BG behavior as discussed in Ref. [81] for the case of random disorder. A Mott glass is a gapless yet incompressible insulator. In Ref. [81] the authors present numerical results which suggest that there exists a region in parameter space where the system possesses Mott-glass-like behavior, i.e. negligible compressibility κ, with $\kappa \sim \exp(-b/T^{\alpha}) + c$ ($\alpha < 1$ and $c \sim 0$). In analogy with [81], I have studied the behavior of κ away from the SF lobe boundary at fixed β as a function of Δ/J, and at fixed Δ/J as a function of β. Figure 5.4 shows κ vs. Δ/J for $U/J = 45$, $L = 21$, and $\beta = L/2$. The compressibility becomes finite at $\Delta/J \sim 23.5$ and plateaus at $\Delta/J \sim 24.5$. Figure 5.6 shows κ as a function of β at $U/J = 45$ and $L = 21$ for Δ/J =22, 23.5, 23.6, 23.7, 23.8, 23.9, and 26. Our data indicates that below the quantum critical point, $\Delta_c/J = 23.76 \pm 0.05$, the system is in the MI state and $\kappa \sim \exp(-\beta\Delta_G)$, where Δ_G is the energy gap. Upon increasing the disorder strength the system enters the BG phase as shown by a plateaued compressibility at large enough β (see curves corresponding to Δ/J =23.9 and 26). It should be noted that at $\Delta/J = 23.8$, I observe MI-like behavior which can be attributed to the finite size of the system. The numerical results shown in Figure 5.4 and 5.6 strongly support the absence of a crossover region where the system behaves like a Mott glass. If this crossover region exists at $U/J = 45$, Figure 5.6 suggests that it would only extend within a range of disorder strength of width $\sim 1\%$.

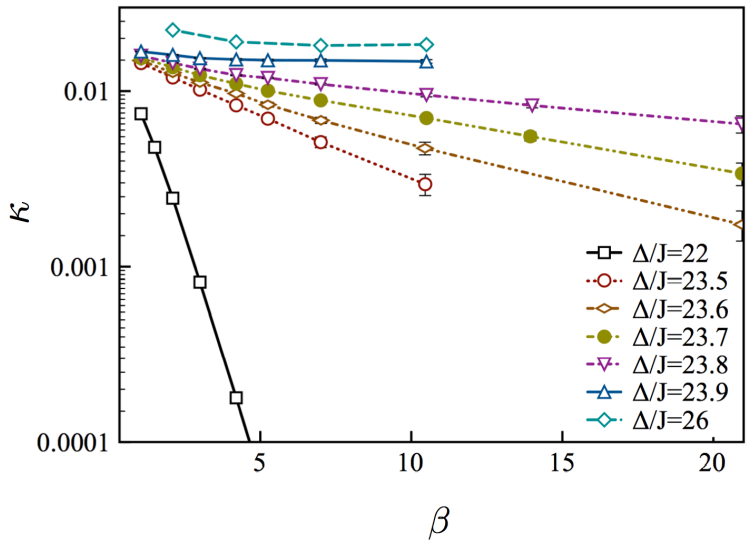

Figure 5.6: The plot shows $\log \kappa$ as a function of β, at $U/J = 45$ and $L = 21$ for Δ/J =22, 23.5, 23.6, 23.7, 23.8, 23.9, and 26. Below the critical point $\Delta/J = 23.76 \pm 0.05$ (see Figure 5.5) the behavior is consistent with that of a MI. Above the transition, the behavior is consistent with that of the BG phase. Error bars are within the symbols if not shown in the figure.

5.4 Conclusion

In conclusion, I have used path integral quantum Monte Carlo by the Worm algorithm to study the phase diagram of bosons in a two-dimensional quasi-periodic optical lattice. As in the case of random disorder, the ground state phase diagram contains three phases: superfluid, Mott insulator, and Bose glass. At weaker interactions, the superfluid phase is favored and significant disorder has to be introduced in order to destroy superfluidity. At strong enough interactions, the superfluid phase has disappeared, and for weak enough disorder the system forms a Mott insulator. Upon increasing the disorder strength the system undergoes a phase transition from Mott insulator to Bose glass. I have used finite temperature simulations to establish that unlike what recently reported for random disorder [81],

there is no Mott-glass-like Bose glass behavior separating the Mott insulator from the Bose glass. Finally, at intermediate interaction strengths and lower disorder, the compressibility of the Bose glass is too small to be measured numerically in finite systems. In this region I am unable to distinguish between a Mott insulator phase and a Bose glass phase.

Chapter 6

Equilibrium phases of dipolar lattice bosons in the presence of random diagonal disorder

6.1 Introduction

In this chapter, I present the numerical results of dipolar bosons in a two-dimensional optical lattice in the presence of a random diagonal disordered potential. The material presented in this chapter is based on my work published in Ref. [51]. The Hamiltonian of the above system is described by the extended Bose-Hubbard model, with an extra term which is the on-site bound disordered potential term.

The work in this chapter focuses on dipolar lattice systems. Right now, dipolar lattice systems are experimentally accessible. They can be realized with polar molecules [36, 85], atoms with large magnetic moments [86, 87], and Rydberg atoms [88, 89, 90]. Unlike single-component atomic systems which are purely interacting via Van-der-Waals interactions, dipolar systems interacting via the long-range and anisotropic dipolar interactions can realize novel superfluid, solid, and topological phases [91, 92, 93, 94, 95, 96, 97]. While in-depth theoretical studies of dipolar lattice bosons in the presence of disorder are still lacking, as suggested in Ref. [98], many of these phases may not be robust in the presence of disorder.

In the following sections, I study the two-dimensional hard-core dipolar bosons

trapped in a square optical lattice and in the presence of random on-site disordered potential. I use large-scale quantum Monte Carlo simulations by the Worm algorithm [76] to study the robustness of the equilibrium phases to disorder. In particular, I show that the interplay of the long-range interactions and the on-site disorder leads to the suppression of the checkerboard (CB) order, while enhancing the superfluid (SF) order, and stabilizing a Bose glass (BG) phase.

6.2 System Hamiltonian

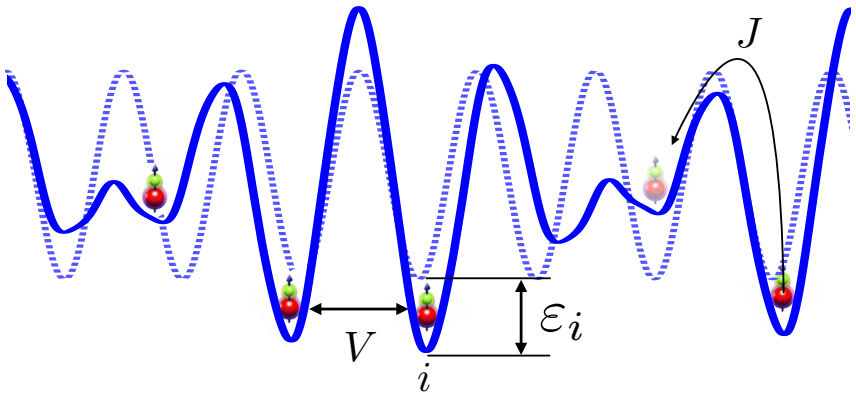

Figure 6.1: Schematic representation of dipolar bosonic lattice system in 1D. The blue dotted line represents the original optical lattice without the disordered potential. The blue solid line represents the optical lattice in the presence of a diagonal disordered potential. The green-red dots are the dipolar bosons.

First, I write down the Hamiltonian of the system. The system is comprised of hard-core, dipolar lattice bosons in a two-dimensional square lattice, with the dipole moments aligned perpendicular to the lattice by an external static electric field so that the dipolar interaction is purely repulsive. At half-integer filling and in the absence of disorder, the system is either in a superfluid (SF) state at

lower dipolar interaction strength or in a checkerboard (CB) solid phase at larger dipolar interaction strength [92]. In the presence of on-site disorder, the system is described by the Hamiltonian:

$$H = -J \sum_{\langle i,j \rangle} a_i^\dagger a_j + V \sum_{i<j} \frac{n_i n_j}{r_{ij}^3} - \sum_i (\varepsilon_i - \mu) n_i \quad , \tag{6.1}$$

where the first term is the kinetic energy characterized by hopping amplitude J. Here, $\langle \cdots \rangle$ denotes nearest neighboring sites, $a_i^\dagger$ (a_i) are the bosonic creation (annihilation) operators satisfying the usual commutation relations and the hard-core constraint $a_i^\dagger a_i^\dagger = 0$. The second term is the purely repulsive dipolar interaction characterized by strength $V = d^2/a^3$, d is the induced dipole moment and a is the lattice spacing, r_{ij} is the relative distance (measured in units of a) between site i and site j, $n_i = a_i^\dagger a_i$ is the particle number operator. The third term is the chemical potential term with chemical potential μ shifted by the on-site random disordered potential ε_i, where ε_i is uniformly distributed within the range $[\Delta, -\Delta]$. I set the unit of energy and length to be the hopping amplitude J and the lattice spacing a, respectively.

Figure 6.1 is a schematic representation of dipolar bosonic lattice system in one dimension. The blue dotted line represents the original optical lattice without the disordered potential. The blue solid line represents the optical lattice in the presence of diagonal disordered potential. The green-red dots are the dipolar bosons. J is the hopping amplitude, V is the dipole-dipole repulsive interaction, and ε_i is the on-site diagonal disordered potential.

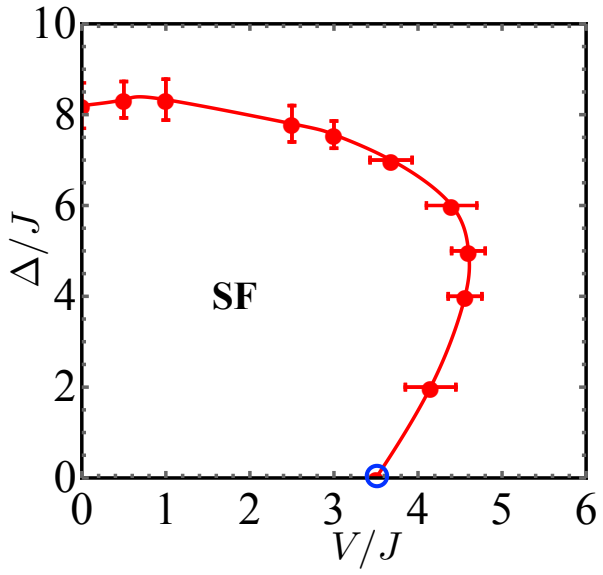

Figure 6.2: Phase diagram of the system described by Equation 6.1 at filling factor $n = 0.5$. The horizontal and vertical axes are the dipole-dipole repulsive interaction strength V/J and the disorder strength Δ/J, respectively. Solid red circles represent superfluid to insulator transition points as determined by standard finite size scaling. The solid line is a guide to the eye. The blue circle is the interaction strength at which superfluidity disappears in favor of a checkerboard solid in the clean system. Error bars are within the symbols if not visible in the plots.

6.3 Ground state phase diagram

In this section, I present the numerical results for the ground state phase diagram of Equation 6.1 at fixed filling factor $n = 0.5$, which is shown in Figure 6.2. The horizontal and vertical axes are the dipole-dipole interaction strength V/J and the disorder strength Δ/J, respectively. Red circles represent SF-insulator transition points. The red solid line is a guide to the eye. At zero disorder, the system is either in the SF phase for $V/J < 3.5$, or the CB phase (blue circle) [92]. The SF phase is characterized by finite superfluid stiffness ρ_s which can be determined from the statistics of winding numbers in space. Specifically, $\rho_s = \langle \mathbf{W}^2 \rangle / dL^{d-2}\beta$, where $\mathbf{W}^2 = W_x^2 + W_y^2$, $W_{x,y}$ being the winding number in spatial directions x

and y, $d = 2$ is the spatial dimension, and β is the inverse temperature [99]. The CB solid possesses diagonal long-range order and is characterized by a finite value of structure factor $S(\mathbf{k}) = \sum_{\mathbf{r},\mathbf{r}'} \exp\left[i\mathbf{k}(\mathbf{r}-\mathbf{r}')\right]\langle n_{\mathbf{r}} n_{\mathbf{r}'}\rangle/N$, here $\mathbf{k}$ is the reciprocal lattice vector. For CB solid, $\mathbf{k} = (\pi, \pi)$.

For $V/J < 3.5$, the SF is destroyed in favor of a BG phase for disorder strength $7 < \Delta/J < 8$. This is in contrast to what was found for the Bose-Hubbard model at unit filling and in the limit of weak interactions where sizable disorder strength $\Delta/J \sim 75$ is needed in order to destroy superfluidity [47]. This can be easily understood as follows. In the weak interaction limit, interactions compete with Anderson localization resulting in an enhancement of superfluidity. Here, instead, the hard-core nature of bosons suppresses superfluidity even at weak dipolar interaction. As a matter of fact, for $V/J < 3.5$ superfluidity is destroyed in favor of the BG at a nearly constant value of disorder strength $7 < \Delta/J < 8$, that is, the critical disorder strength is nearly independent of the dipolar interaction strength. Furthermore, at finite disorder strength $\Delta/J \lesssim 7$, the SF phase persists for dipolar interaction $V/J > 3.5$, whereas the clean system featured a CB solid at this point. I attribute this to the competition between dipolar interaction which favors the CB order and disorder which tends to destroy it, resulting in a superfluid phase persisting beyond $V/J \sim 3.5$. Superfluidity is eventually completely destroyed for $V/J \gtrsim 4.6$.

With the exception of the transition point corresponding to $\Delta/J = 2.0$, the SF to insulator transition appears to be of second order as demonstrated by the finite-size scaling of the superfluid stiffness ρ_s where I have used the dynamical

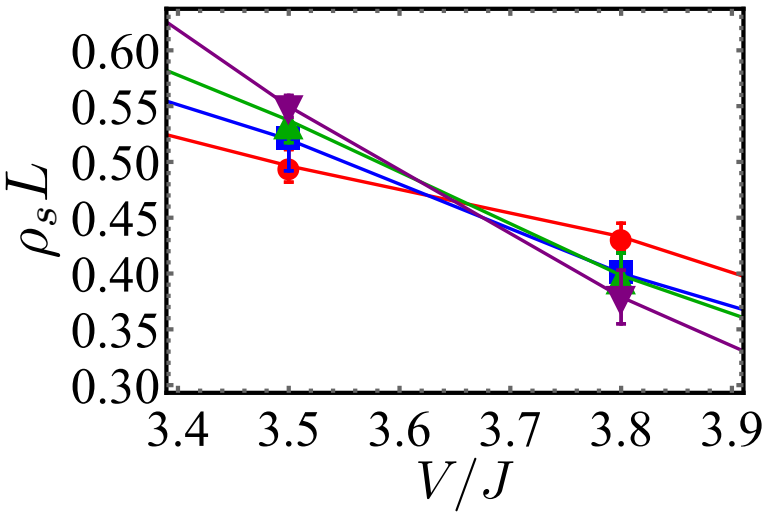

Figure 6.3: Finite size scaling of the superfluid stiffness ρ_s. I plot $\rho_s L$ vs. V/J at $\Delta/J = 7$ for system sizes $L = 12$, 16, 20, and 24 (red circles, blue squares, green up triangles, and purple down triangles, respectively). The transition point corresponds to the value of V/J where curves referring to different system sizes cross. Here, $V_c/J = 3.68 \pm 0.25$. Error bars are within the symbols if not visible in the plots.

critical exponent $z = 1$ (see Figure 6.3). For each V/J and Δ/J, I average over 500-1000 realizations of disorder, with disorder strength uniformly and randomly distributed within the interval $[-\Delta, \Delta]$. I have used system sizes $L = 12$, 16, 20, and 24. The transition point corresponds to the value of V/J where curves referring to different system sizes cross ($V_c/J = 3.68 \pm 0.25$ in this example). I note that even for $V/J > 3.5$ the SF disappears in favor of the BG phase rather than a first-order phase transition to the diagonally ordered CB phase. This is further confirmed by the observation of finite compressibility $\kappa = \beta(\langle n^2 \rangle - \langle n \rangle^2)$, measuring density fluctuations, across the transition (see below).

The computational cost of the simulations limit to system sizes of $L = 100$. As such, I am unable to perform finite size scaling at fixed $\Delta/J = 2$, and estimate the transition point to be within the range delimited by the interaction value

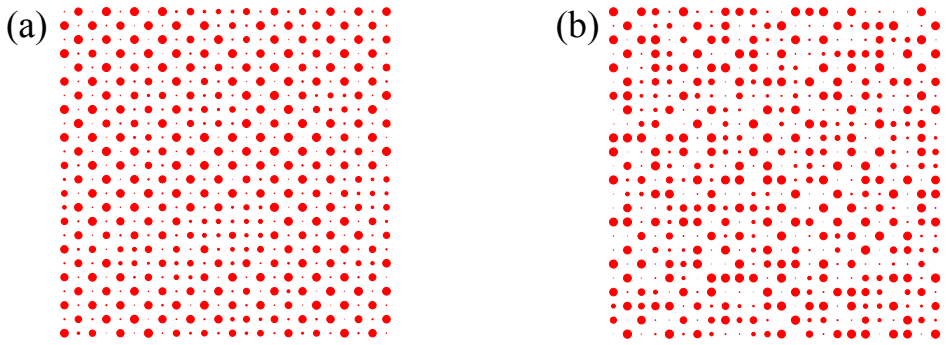

Figure 6.4: Imaginary-time average of the density distribution for a given Monte Carlo configuration and a specific disorder realization at (a) $V/J = 4.2$, $\Delta/J = 2$, (b) $V/J = 4.0$, $\Delta/J = 7$.

where I start seeing finite size effects and the interaction value at which ρ_s for the largest L ($L = 100$) goes to zero. Unlike what I observed for larger values of disorder strength, at $\Delta/J = 2$ the superfluid phase is destroyed in favor of an insulating phase where the CB pattern is stabilized everywhere in the lattice apart from small superfluid regions. This can be seen in Figure 6.4(a), where I plot the imaginary-time average of the density distribution for a given Monte Carlo configuration and for a specific disorder realization at $V/J = 4.2$, $\Delta/J = 2$. Here, the radius of each circle is proportional to the density at that site. For comparison, in Figure 6.4(b), I show the density map at $V/J = 4.0$, $\Delta/J = 7$ where the CB patterns are clearly absent. While I observe coexistence of the SF and CB phases, our present results do not allow us to determine the nature of the SF-insulator transition. Figure 6.4(a) seems to suggest that a BG phase no longer intervenes between the SF and the CB phase but rather the SF phase directly disappears in favor of a "disordered" CB pattern. Due to computational

limitations though, I am unable to determine the existence of a direct SF-CB phase transition for disorder strength $\Delta/J < 4$.

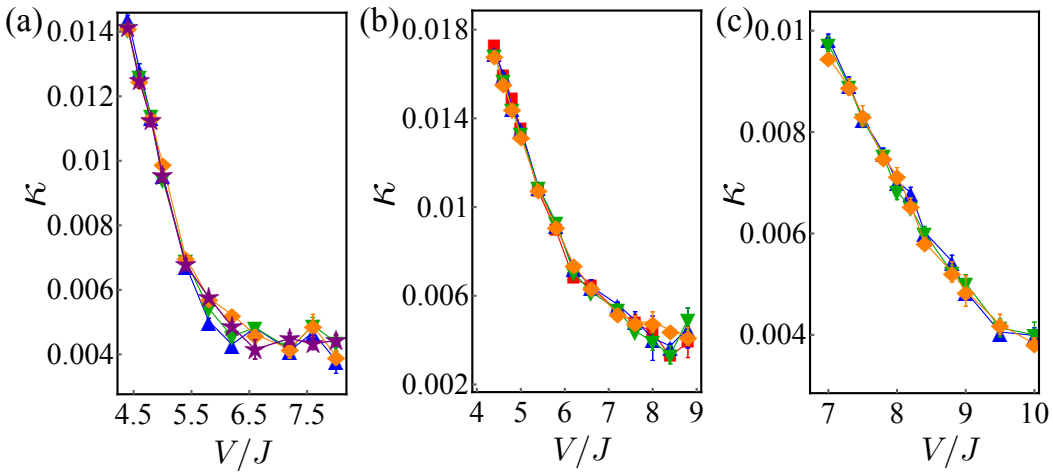

Figure 6.5: Compressibility κ as a function of V/J for system sizes $L = 12$, 16, 20, 24, and 28 (red squares, blue up triangles, green down triangles, orange diamonds, and purple stars, respectively) at fixed disorder strength $\Delta/J = 4$ (a), 5 (b) and 7 (c). Compressibility remains finite beyond the superfluid to insulator transition confirming that the superfluid phase disappears in favor of a Bose glass. At large enough interaction, κ seems to plateau. Upon approaching the plateau, extended CB patterns appear in the density distribution (see text for details). Error bars are within the symbols if not shown in the figures.

As the dipolar interaction strength is increased at fixed disorder strength, one expects the BG to eventually disappear in favor of the CB solid, the latter being characterized by diagonal long range order and zero compressibility. I have performed scans in interaction strength at fixed Δ/J. Figure 6.5 shows compressibility κ as a function of V/J at fixed $\Delta/J = 4$, 5, and 7 (Figure 6.5(a), (b), and (c), respectively) for system sizes ranging from $L = 12$ to 28. I identify the SF to insulator transition points for $\Delta/J = 4$, 5, and 7 to be at $V/J = 4.56 \pm 0.2$, 4.6 ± 0.2, and 3.68 ± 0.25, respectively. Clearly, the compressibility remains finite beyond the transition confirming that the SF disappears in favor of a BG, rather

than the CB solid. Notice that at a given interaction strength, κ is larger for larger disorder strength. Indeed, in this region of the parameter space, disorder competes with interactions which stabilize the incompressible CB solid. The larger the disorder strength, the larger the interaction strength needed in order to observe extended CB patterns in the density distribution. As expected, in all cases, compressibility decreases as interaction increases. At large enough interaction, κ seems to plateau. The larger the Δ/J, the larger the interaction at which the plateau is observed. Upon approaching the plateau, extended CB patterns appear in the density distribution. However, due to the presence of disorder, defects and grain boundaries persist even at increasing interaction strengths and contribute to a small residual compressibility. In Figure 6.6(a) I plot the imaginary-time average of the density distribution for a given Monte Carlo configuration and for a specific disorder realization at $V/J = 10.0$, $\Delta/J = 7.0$. For comparison, I show the density maps in the BG phase at $V/J = 4.5$, $\Delta/J = 7.0$ (Figure 6.6(b)) and at $V/J = 1.0$, $\Delta/J = 9.5$ (Figure 6.6(c)). For $V/J > 3.5$, a specific disorder realization featuring regions that locally mimic a clean system allows the dipolar interactions to stabilize the CB phase in those regions. Such islands of CB phase are observed in Figure 6.6(b), but are absent from Figure 6.6(c) where the strength of interactions, $V/J < 3.5$ is below the critical strength required to stabilize the CB phase in the clean system. I note that the disappearance of the BG in favor of a CB solid happens over a range of increasing V/J values at a fixed Δ/J. As V/J increases, islands of CB within the BG phase grow larger and eventually the system settles into a CB with localized defects.

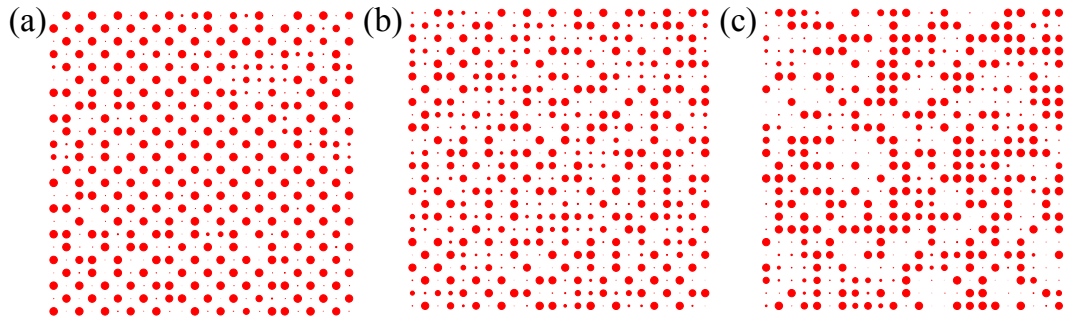

Figure 6.6: Imaginary-time average of the density distribution for a given Monte Carlo configuration and a specific disorder realization at (a) $V/J = 10.0$, $\Delta/J = 7.0$, (b) $V/J = 4.5$, $\Delta/J = 7.0$, and (c) $V/J = 1.0$, $\Delta/J = 9.5$. The radius of each circle is proportional to the density at that site. Defects and grain boundaries within the checkerboard order are present in (a). They contribute to a small residual compressibility.

6.4 Finite temperature results

In this section, I investigate the robustness of the SF state against thermal fluctuations. Upon increasing the temperature, thermal fluctuations destroy superfluidity via a Kosterlitz-Thouless (KT) transition [100]. In the following, I fix interaction strength to $V/J = 2$ and scan over disorder strength to find the critical temperature at which the SF disappears. Figure 6.7 shows the critical temperature T_c/J as a function of Δ/J. Figure 6.8(a) shows the ground state compressibility κ as a function of disorder strength Δ/J for $L = 24$. Figure 6.8(b) shows the ground state superfluid stiffness ρ_s vs. Δ/J for $L = 24$. While compressibility does not change significantly, ρ_s is suppressed as disorder strength is increased. As a result, the corresponding critical temperature decreases as a function of Δ/J, as seen in Figure 6.7. The critical temperature is found using standard finite size scaling. In the thermodynamic limit, a universal jump is

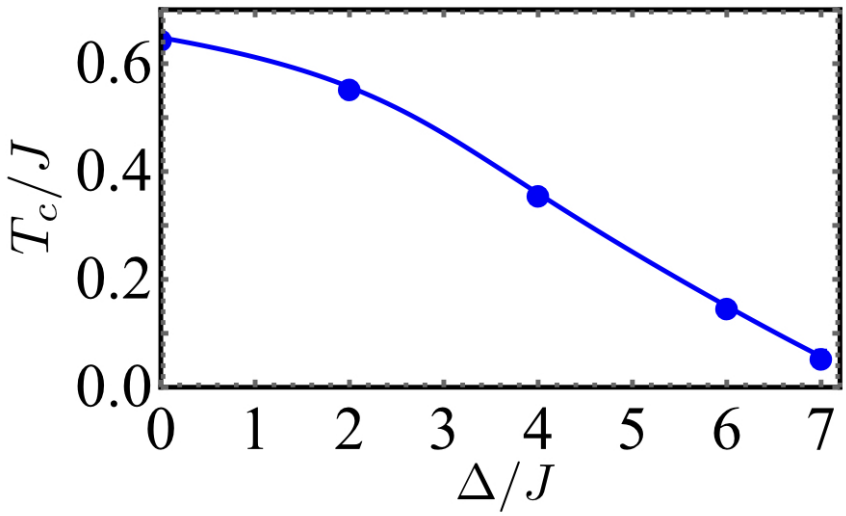

Figure 6.7: This plot refers to $V/J = 2$. Critical temperature T_c/J for disappearance of superfluidity via a KT transition as a function of Δ/J. Error bars are within symbol size if not visible in the plots.

observed at a critical temperature given by $\rho_s(T_c) = 2mk_BT_c/\pi\hbar^2$. In a finite size system this jump is smeared out, as seen in Figure 6.9(a), which shows ρ_s as a function of T/J at $\Delta/J = 4$ for system sizes $L = 12$, 16, 20, 24, 36, and 60. The dotted line in Figure 6.9(a) corresponds to $\rho_s = T/\pi$ and its intersection points $T_c(L)/J$ with each ρ_s-vs.-T/J-curve are used to find T_c/J as shown in Figure 6.9(b). Here, I plot $T_c(L)/J$ vs. $1/\ln^2 L$ and find the critical temperature at $\Delta/J = 4$ to be $T_c/J \sim 0.36$. Finally, I note that the critical interactions strengths corresponding to the stabilization of each equilibrium phase are achievable in current experiments. However, further improvements will be needed, both in cooling and loading phases, to achieve the required lattice gas temperatures.

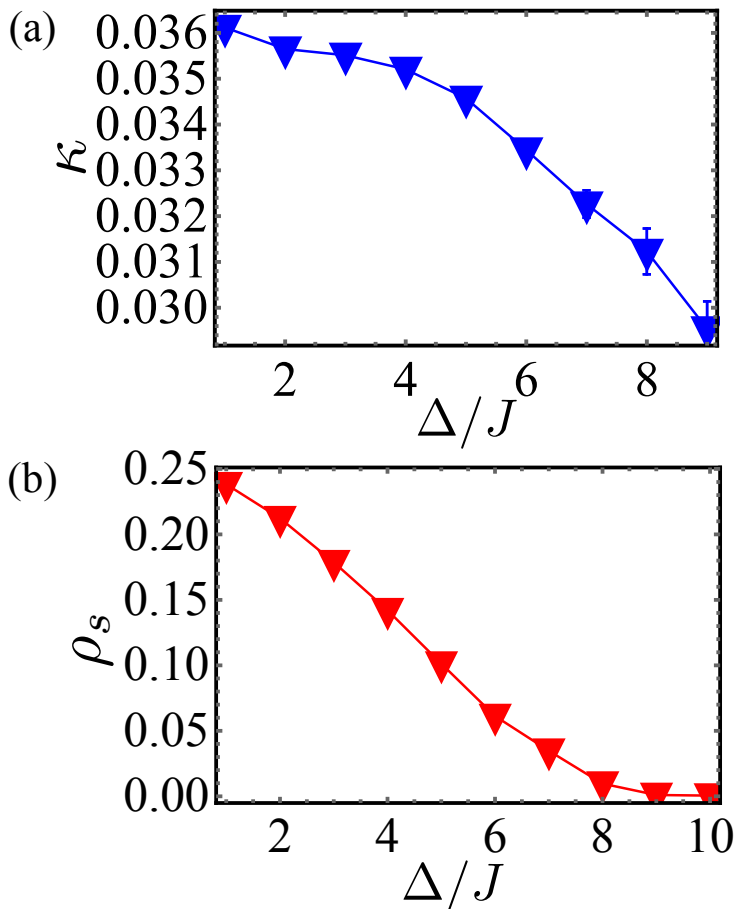

Figure 6.8: This plot refers to $V/J = 2$. (a) Superfluid stiffness ρ_s as a function of Δ/J for system size $L = 24$. (b) Compressibility κ as a function of Δ/J for system size $L = 24$. Error bars are within symbol size if not visible in the plots.

6.5 Conclusion

I have studied hard-core bosons trapped in a square lattice, interacting via purely repulsive dipolar interaction and in the presence of on-site bound disorder. Our results are based on large-scale path integral quantum Monte Carlo simulations by the Worm algorithm. I have presented the ground state phase diagram at fixed half-integer filling factor for which the clean system is a superfluid at lower dipolar interaction strength and a checkerboard solid at larger dipolar interaction strength. I find that, even for weak dipolar interaction, superfluidity is destroyed

in favor of a Bose glass at relatively low disorder strength. This is in contrast to what found for the Bose-Hubbard model at fixed unity filling and in the limit of weak interactions where sizable disorder strength is needed in order to destroy superfluidity. This can be explained by the hard-core nature of bosons which suppresses superfluidity even at weak dipolar interaction. Interestingly, in the presence of disorder, superfluidity persists for values of dipolar interaction strength for which the clean system is a checkerboard solid. At fixed disorder strength, as the dipolar interaction is increased, superfluidity is destroyed in favor of a Bose glass. As the interaction is further increased, the system eventually develops extended checkerboard patterns in the density distribution. Due to the presence of disorder, though, grain boundaries and defects, responsible for a finite residual compressibility, are present in the density distribution. Finally, I have studied the robustness of the superfluid phase against thermal fluctuations where I found that, at fixed dipolar interaction, the critical temperature at which superfluidity disappears decreases as the disorder strength increases.

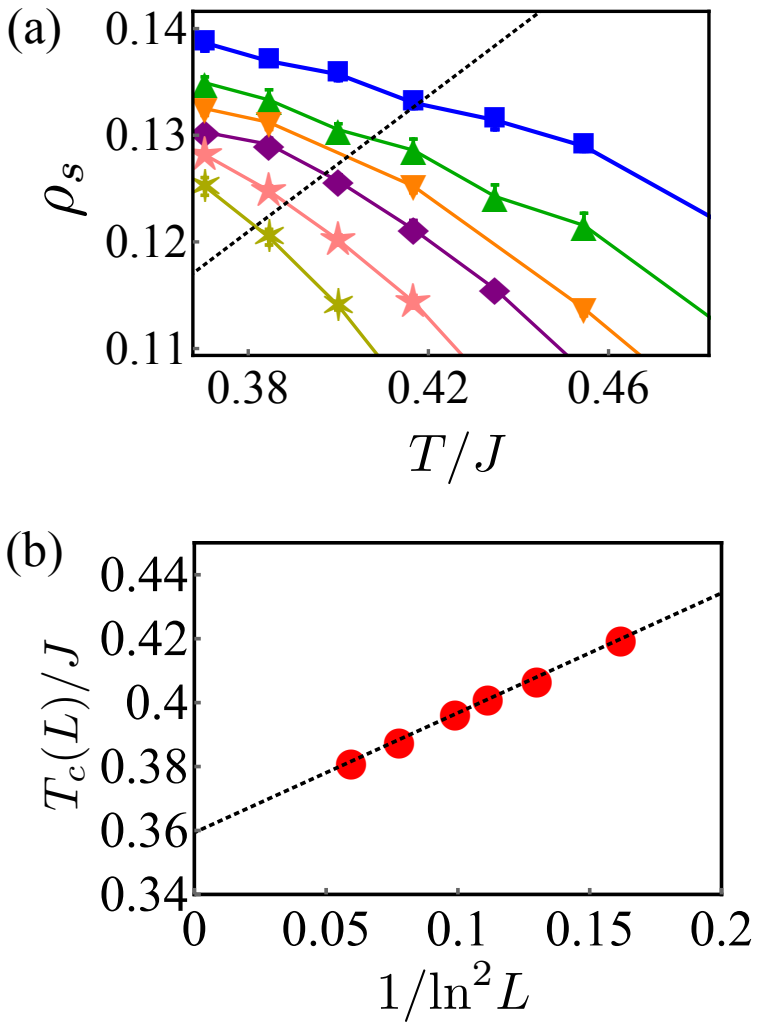

Figure 6.9: (a) Superfluidity ρ_s as a function of T/J for $L = 12$, 16, 20, 24, 36, and 60 (blue squares, green up triangles, purple down triangles, orange diamonds, pink stars, and yellow asterisks, respectively), at $\Delta/J = 4$. Dotted line corresponds to $\rho_s = T/\pi$. Its intersection points with each ρ_s-curve give "critical" temperatures $T_c(L)/J$ for a finite system. (b) $T_c(L)/J$ vs. $1/\ln^2 L$. Error bars are within symbol size if not visible in the plots.

Chapter 7

Quantum Monte Carlo study of the long-range site-diluted XXZ-model as realized by polar molecules

7.1 Introduction

In this chapter, I present the quantum Monte Carlo study of the long-range site-diluted XXZ-model, which can be realized using polar molecules in cold atom experiments. The material presented in this chapter is based on my work published in Ref. [52]. Interacting bosons in the presence of disorder have attracted a great deal of attention in the past decades. Disorder can be found or engineered in a variety of systems, ranging from ^{4}He in porous media and aerogels [101, 24, 102], thin superconducting films [25, 103, 17], Josephson-junction arrays [26], to ultracold gases [19, 28, 6]. Diagonal disorder has been extensively studied in theory and experiment. In theory, the compressible gapless Bose glass phase, intervening between the Mott insulator and the superfluid phase in the presence of diagonal disorder, has been investigated in great detail using a variety of different methods such as density matrix renormalization group [45], Monte Carlo simulations [46, 8, 7, 47, 48, 49], and mean field theory [50]. Diagonal disorder has also been studied in the presence of long-range hopping. Depending on the ratio between the power-law decay of the hopping and the dimensionality of the system, the combination of on-site disorder and long-range hopping may result in localization, critical behavior or fully extended states [104]. On the other

hand, systems exhibiting off-diagonal disorder have received less attention. As an example, it has been shown that in the presence of off-diagonal disorder, the incompressible yet gapless Mott glass phase intervenes between the Mott insulator and the superfluid phase [105, 106, 107, 108]. When both, off-diagonal long-range interaction and off-diagonal disorder are present, the interplay between the two may result in new interesting phenomena.

Purely off-diagonal disorder in systems exhibiting long-range hopping and interactions have recently been realized experimentally with polar molecules trapped in deep optical lattices [36, 85]. A spin 1/2 degree of freedom is encoded in two internal states of the molecules (the lowest rovibrational state and an excited rotational state) which are coupled via a microwave field. Molecules are pinned to lattice sites due to the deep optical lattice while the dipolar interaction induces spin exchanges between pairs of molecules. At integer unit filling, and in the presence of an external dc electric field, this system realizes a spin XXZ model where the effective magnetic interactions decay as $\frac{1}{r^3}$ where r is the distance between lattice sites [85]. Spin-spin interactions can be tuned with the external electric field but they can also be modified by choosing different pairs of rotational levels. In a typical experiment, not all sites are occupied, but rather, sites are randomly filled by a single molecule or are unoccupied. Recent experiments report a filling fraction of 25% [109]. This results in the presence of disorder in the long-range spin-exchange term (equivalent to long-range hopping). Since the configuration of occupied sites varies in the experiments from shot to shot, experimental measurements are effectively averaging over different disorder

realizations. Recently, this system has been studied in the case of a single spin-excitation present [110, 111]. The authors found that localization of eigenstates depends on dimensionality and filling. While these results can be extended to the case of a dilute gas of excitations, the full many-body case has yet to be studied.

Here, I study the long-range XXZ model in the presence of off-diagonal disorder. I find that, unlike what observed in the case of short-range interactions, localization never occurs even for site dilution larger than the percolation threshold and off-diagonal order, though strongly suppressed, persists for arbitrarily large values of site dilution.

7.2 System Hamiltonian

In the following, I study the two-dimensional spin 1/2 XXZ model defined on a square lattice, as realized by polar molecules trapped in deep optical lattices. The spin 1/2 degree of freedom is encoded in two rotational states coupled via a microwave field. Hopping is suppressed and at most a single molecule occupies each lattice site. The model reads as

$$H = \sum_{i,j} \Big[\frac{J_{ij}^{\perp}}{2} (S_i^+ S_j^- + S_i^- S_j^+) + J_{ij}^z (S_i^z S_j^z) \Big] \quad . \tag{7.1}$$

Here $S_i^{\pm}$ and S^z are the spin 1/2 operators which obey $[S_i^z, S_j^{\pm}] = \pm \delta_{ij} S_i^{\pm}$; the spin-exchange interaction $J_{ij}^{\perp} = \frac{J_{\perp}}{r_{ij}^3}$ with $J_{\perp} < 0$; $J_{ij}^z = \frac{J_z}{r_{ij}^3}$ is the strength of the spin-spin repulsion; r_{ij} is the relative distance between site i and site j. Note that the Ising term, with coupling strength J_z, is present only if an external dc electric

field (parallel to the quantization axis) is applied. Equation 7.1 features purely off-diagonal disorder resulting from randomly distributed unoccupied lattice sites.

Equation 7.1 can be exactly mapped onto a site-diluted model of hardcore lattice bosons in the presence of long-range dipolar hopping and dipolar interaction [112]:

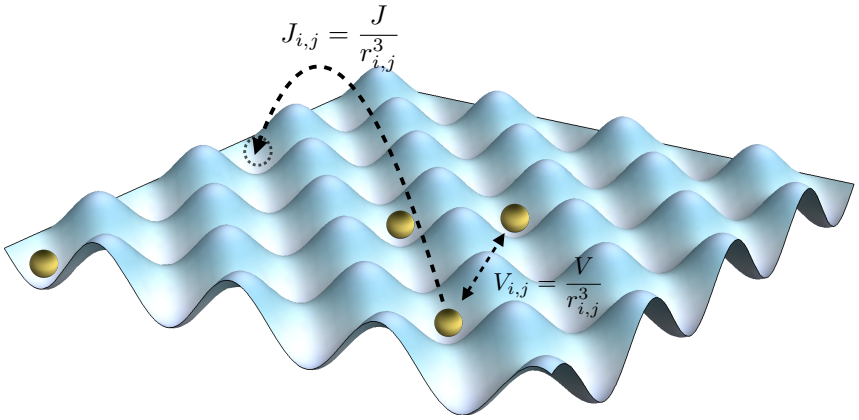

Figure 7.1: Schematic representation of dipolar lattice system. The 2D optical lattice is generated by crossing two laser standing waves perpendicularly. The brass-tone balls are dipolar bosons.

$$H = -J \sum_{i<j} \frac{1}{r_{ij}^3} (a_i^\dagger a_j + a_i a_j^\dagger) + V \sum_{i<j} \frac{n_i n_j}{r_{ij}^3} \quad , \tag{7.2}$$

where $\frac{J_\perp}{2} = -J$, $J_z = V$. The first term in the Hamiltonian is the kinetic energy, where $a_i^\dagger$ (a_i) are the bosonic creation (annihilation) operators on the site i satisfying usual commutation relations and the hard-core constraint $a_i^\dagger a_i^\dagger = 0$. J is the hopping amplitude with hopping matrix element $J_{ij} = \frac{J}{r_{ij}^3}$, where r_{ij} is the relative distance between site i and site j. The second term describes the dipole-dipole purely repulsive interaction with strength V and $V_{ij} = \frac{V}{r_{ij}^3}$. Site-dilution corresponds to removing a certain fraction of sites from the lattice, which, in

the experimental setup, correspond to unoccupied sites. Site-dilution results in off-diagonal disorder.

In the following, I perform large-scale quantum Monte Carlo simulations by the Worm algorithm to study equilibrium phases of Equation 7.2 both for the clean case and in the presence of disorder.

7.3 Ground state phase diagram in absence of site dilution

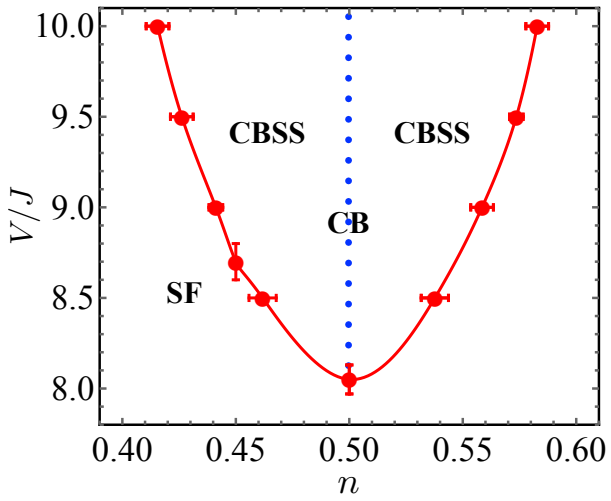

Figure 7.2: Ground state phase diagram of Equation 7.2 as a function of interaction strength V/J and filling factor n. The system features three phases: a superfluid phase (SF), a checkerboard solid phase (CB) and a checkerboard supersolid phase (CB SS). At half filling, the SF is destroyed in favor of a CB via a first order phase transition. At $V/J > 8$, the CB SS can be reached by doping the CB solid with particles or holes. At large enough doping, the CB SS gives way to a SF via a second order phase transition. Red circles are numerical results for the SF to CB SS second order transition. Blue dotted line indicates CB at half filing. Error bars are within the symbols if not shown in the figure.

In this section, I study the phase diagram of Equation 7.2 in the absence of site dilution. The phase diagram is shown in Figure 7.2 in the plane of V/J vs. n, the filling factor. I find that, for large enough interaction, three phases

are stabilized: a superfluid phase (SF), characterized by off-diagonal long-range order, a checkerboard solid phase (CB), characterized by diagonal long-range order, only present at density $n = 0.5$, and a checkerboard supersolid phase (CB SS), characterized by both diagonal and off-diagonal long-range order, which can be reached by doping the CB phase away from half-filling. On the other hand, at lower interaction strength, the system is in a SF phase for any value of the filling factor. In spin language, the CB order corresponds to the easy-axis antiferromagnetic order, the SF phase corresponds to easy-plane ferromagnetic order while densities other than 0.5 correspond to the presence of an external magnetic field. The SF phase possesses finite superfluid density ρ_s, easily accessible in our simulations. Notice that, since the hopping term in Equation 7.2 is not limited to nearest neighbors, the standard expression of superfluid density in terms of winding numbers [75] must be generalized [113]. The CB solid is characterized by a finite value of structure factor $S(\mathbf{k}) = \sum_{\mathbf{r},\mathbf{r}'} \exp\left[i\mathbf{k}(\mathbf{r}-\mathbf{r}')\right]\langle n_{\mathbf{r}} n_{\mathbf{r}'}\rangle/N$, $\mathbf{k}$ is the reciprocal lattice vector with $\mathbf{k} = (\pi, \pi)$ in the CB. Finally, the CB SS is characterized by finite ρ_s and $S(\pi, \pi)$. Compared to the case of nearest-neighbor hopping only, in the presence of long-range hopping, the SF phase is much more robust against interaction strength. Indeed, at $n = 0.5$, the CB phase (blue dotted line in Figure 7.2) is reached for interaction $V/J \sim 8$ compared to $V/J \sim 3.5$ [92] in the nearest-neighbor hopping case. Because the presence of long-range hopping breaks down the sublattice invariance, the transition from SF to CB does not happen via the Heisenberg point but rather it is expected to be of first order (both SF and CB are broken-symmetry states). Our simulations results confirm this

expectation as shown in Figure 7.3 where I show the hysteresis curve for ρ_s (red down triangles) and $S(\pi, \pi)$ (blue up triangles) as a function of V/J for system size $L = 32$.

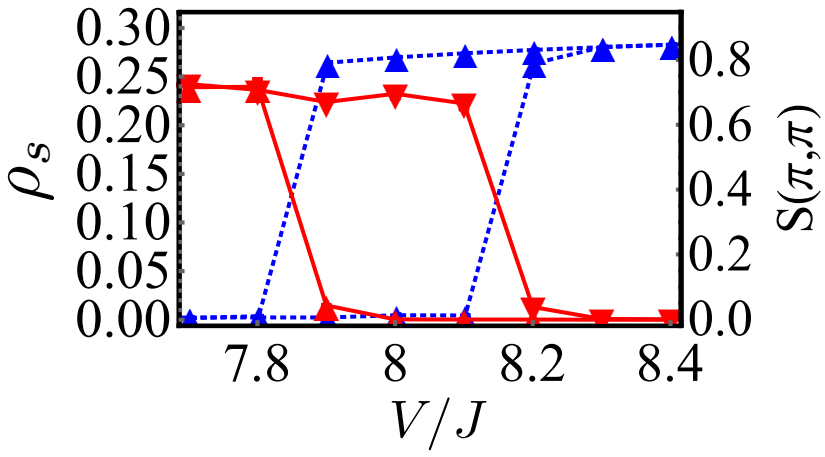

Figure 7.3: Hysteresis curves for ρ_s (red down triangles) and $S(\pi, \pi)$ (blue up triangles) as a function of V/J for system size $L = 32$ signaling a first-order CB-SF phase transition at $n = 0.5$. Error bars are within the symbols if not shown in the figure.

For interaction strength $V/J > 8$, one would expect the CB to give way to the SF phase either via a first order phase transition, which would imply coexistence of CB and SF order, or via a CB SS. I have observed a stable CB SS as demonstrated by the lack of hysteresis in the density n vs. chemical potential μ at fixed V/J. Moreover, as shown in Figure 7.4 for $V/J = 9.0$, n is a smooth function of μ. The CB SS can be reached by doping the CB solid with particles or holes (particle-hole symmetry exists since bosons are hardcore). At large enough doping, the CB SS disappears in favor of a SF via a second order phase transition belonging to the (2+1)-dimensional Ising universality class. Standard finite size scaling is used to

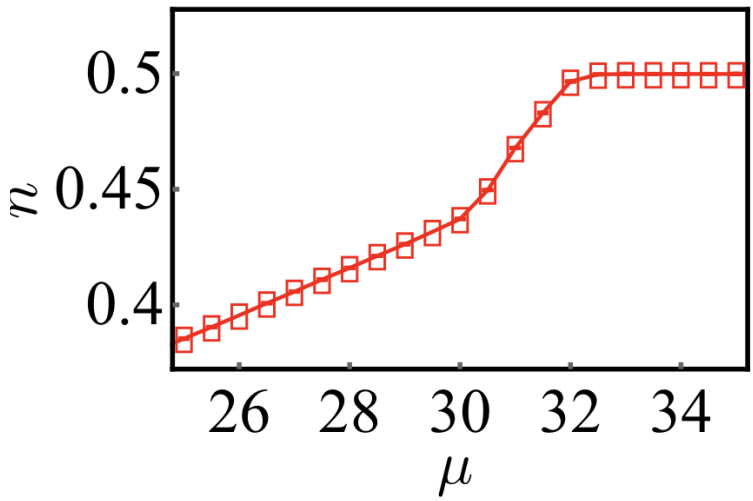

Figure 7.4: Density n as a function of the chemical potential μ for $V/J = 9.0$. Error bars are within the symbols if not shown in the figure.

extract transition points (red circles in Figure 7.2) as shown in Figure 7.5 where I plot $S(\pi, \pi)L^{1.0366}$ vs. filling factor n at fixed interaction strength $V/J = 10.0$ for system sizes $L = 20$, 24, 28, and 32. The crossing of curves corresponding to different system sizes signals the transition, in this case at $n = 0.4147 \pm 0.005$.

7.4 Finite temperature results

In this section, I investigate the robustness of quantum phases against thermal fluctuations. At given $V/J = 9$, I find critical transition temperatures for three above quantum phases to normal fluid phase at the filling factor $n = 0.5$, 0.47, and 0.4, where the system is deep in CB, CB SS, and SF phase, respectively. At half filling, the CB phase will melt to the normal fluid phase when temperature increases. It belongs to 2-dimensional Ising type transition. Figure 7.6(a) shows finite size scaling method which is used to find the critical transition temperature.

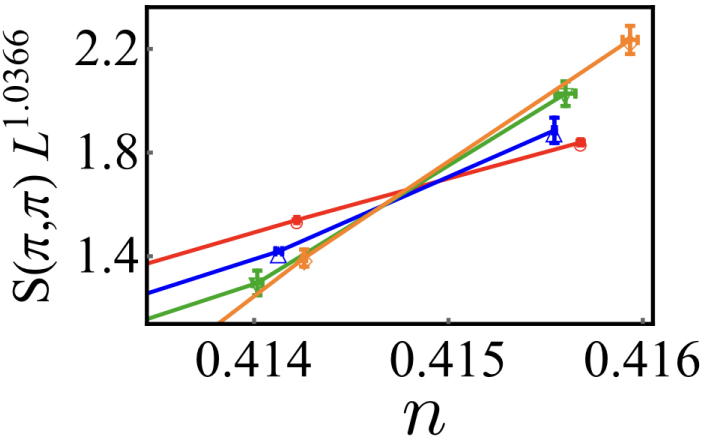

Figure 7.5: Finite size scaling of $S(\pi, \pi)$ at fixed $V/J = 10.0$ for system size $L =$ 20, 24, 28, and 32 (red circles, blue up triangles, green down triangles, and orange diamonds, respectively). The crossing of different curves marks the transition point at $n = 0.4147 \pm 0.005$. Error bars are within the symbols if not shown in the figure.

I plot the scaled structure factor $S(\pi, \pi)L^{0.25}$ as a function of temperature T for different system sizes $L = 24$, 28, and 32 (red circles, blue squares, and green diamonds) at the filling factor $n = 0.5$. The crossing point indicates the transition temperature is $T_c = 2.286 \pm 0.005$. At filling factor $n = 0.47$, the CB SS phase will melt to the normal fluid phase when temperature increases. It belongs to 2-dimensional Ising type transition. The critical temperature $T_c = 1.914 \pm 0.006$ is found by using the same finite size scaling method described above. At filling factor $n = 0.4$, upon increasing temperature, thermal fluctuations will destroy the SF phase in favor of normal fluid phase via a Kosterlitz-Thouless (KT) transition [100]. Figure 7.6(b) shows superfluid density ρ_s as a function of T/J for different system sizes $L = 28$, 32, 36, 60, and 84 (blue squares, green triangles up, orange triangles down, purple diamonds, and brown stars). At thermodynamic limit, there will be a universal jump at critical temperature $\rho_s(T_c) = 2mk_BT_c/\pi\hbar^2$.

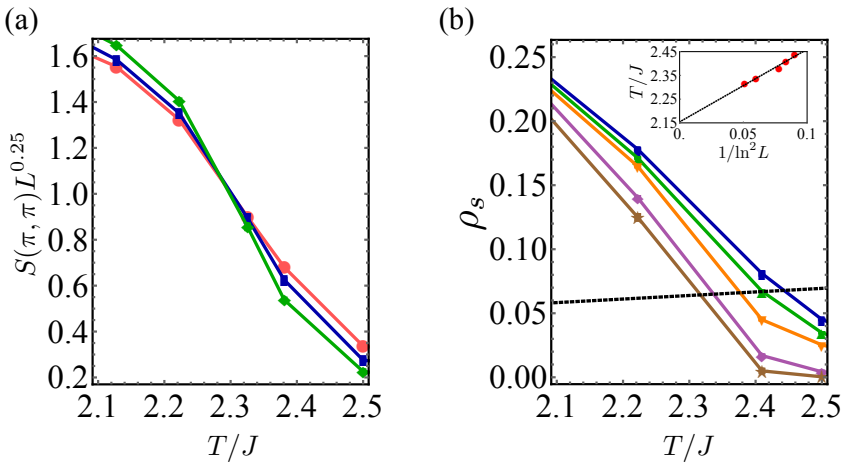

Figure 7.6: (a) The scaled structure factor $\rho_s L^{0.25}$ as a function of T/J for $L = 24$, 28, and 32 (red circles, blue squares, and green diamonds) at filling factor $n = 0.5$. The crossing determines the critical temperature $T_c = 2.286 \pm 0.005$. (b) shows ρ_s as a function of T/J for $L = 28$, 32, 36, 60, and 84 (blue squares, green triangles up, orange triangles down, purple diamonds, and brown stars), at filling factor $n = 0.4$. The dashed line is given by $2mT/\pi$. The insert shows that the intersection points between $2mT/\pi$ line and ρ_s versus T/J curves at each L is used to extract critical temperature $T_c/J \sim 2.15$. Error bars are within the symbols if not shown in the figures.

To get the critical temperature, I plot the line $2mT/\pi$, where $k_B = 1$, $\hbar = 1$, and $m = 0.00436$. I extract the crossing points between $2mT/\pi$ and ρ_s for different system sizes. By plotting $1/\ln^2 L$ as a function of $T(L)$, I find the critical temperature is $T_c/J \sim 2.15$.

To make simulations run faster, I have set cutoff to 8 for both the long-range hopping term and interaction term. Cutoff equal to 8 means that particles hopping to distance $r_{ij} = |\vec{r}_i - \vec{r}_j| \leq 8$ are considered. I checked cutoff as a function of transition points at two filling factors $n = 0.5$ and $n = 0.45$. The former one is the first order phase transition from SF to CB phase. The latter one is the second order phase transition from CB SS to SF phase. Now, I need to check whether the cutoff equals 8 is enough for the simulations. First, I fix the filling factor $n = 0.5$,

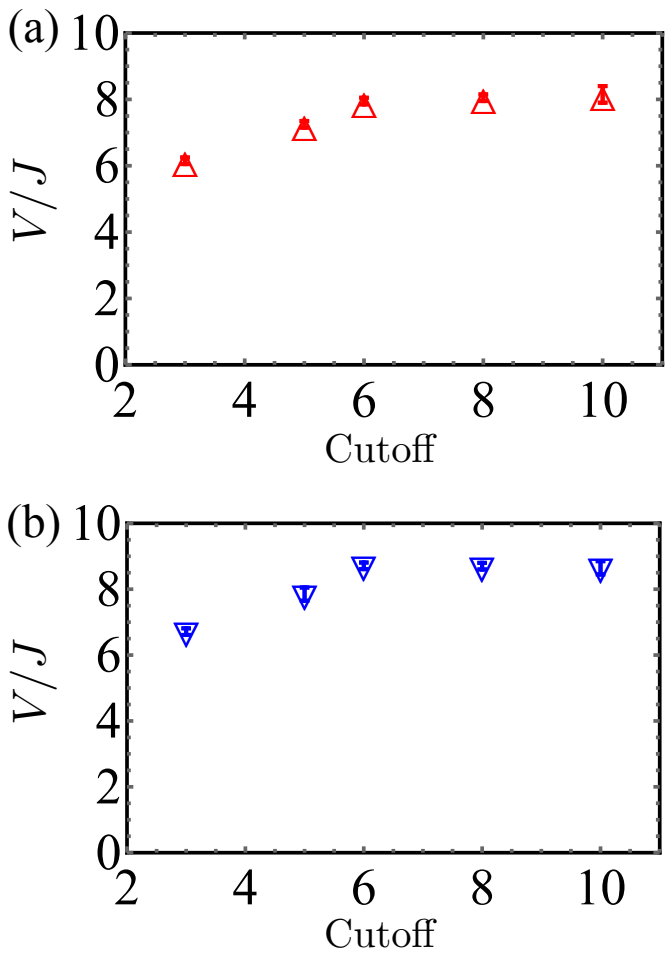

Figure 7.7: The cutoff as a function of transition points V/J at two filling factors (a) $n = 0.5$ and (b) $n = 0.45$. At $n = 0.5$, the SF to CB phase transition is the first order phase transition. At $n = 0.45$, the CB supersolid to SF phase transition is the second order phase transition.

where it is the first order phase transition between the SF and CB solid phase. By plotting ρ_s and $S(\pi, \pi)$ for different system sizes, I find the critical transition points V/J as a function of different cutoffs. Figure 7.7(a) shows the critical transition points as a function of different cutoffs. It can be seen from the plot, when the cutoff is larger than 6, the critical points have the same values within the errorbars. Then, I fix the filling factor $n = 0.45$. At a large enough V/J, the CB SS to SF phase transition belongs to 3-dimensional Ising type transition.

Finite size scaling method is used to determine the critical transition points V/J for different cutoffs. Figure 7.7(b) shows critical transition points as a function of different cutoffs at filling factor $n = 0.45$. When the cutoff is larger than 6, the critical points have the same values within the errorbars. This means the cutoff equal to 8 is enough for our model and using a larger cutoff will not change the simulation results within the errorbars.

I conclude this section by considering the robustness of the quantum phases observed against thermal fluctuations. I have performed finite-temperature simulations at fixed $V/J = 9.0$. The critical temperature for SF-to-normal and CB-to-normal transitions at densities $n = 0.4$, 0.47, and 0.5, corresponding to SF, CB SS, and CB phase at $T = 0$ respectively, are all of the order of $T_c/J \sim 2$. For $J = 104h$ Hz and $V = 0$ as in Ref. [36], this translates to a normal-to-SF transition temperature of about 10.0 nK.

7.5 Site-diluted XXZ model

In this section, I study Equation 7.2 in the presence of site dilution. Because hopping is long-ranged, arguments based on percolation theory (see e.g., [108]) are inapplicable and the presence of an insulating phase beyond the percolation threshold is no longer guaranteed. In the following, I fix the density of the system at $n = 0.5$ (calculated with respect to available sites) and investigate localization of particles upon increasing site dilution p at given values of the interaction $V/J = 0$, 2, and 7, which all correspond to a SF phase in the clean

system. In all cases, temperature has been chosen in order to ensure that the system is in its ground state, i.e., $\beta = \frac{5}{6}L$ with $L = 84$, 100, and 150. As a reminder, site-dilution results from unoccupied sites in the experimental setups. Averaging over different realizations of site dilution corresponds to averaging results from different experimental shots. The simulation results shown below are based on 50-100 realizations of site dilution, depending on the value of the interaction and site dilution. In order to see whether superfluidity is destroyed at large enough site dilution, I look at the spatial decay of the off-diagonal correlator $f_{ij} \propto \sum_{\tau,\tau'} \langle a_i(\tau) a_j^\dagger(\tau') \rangle$, where $a_i(\tau)$, $a_j^\dagger(\tau')$ are annihilation and creation bosonic operators expressed in the interaction picture. In the SF phase, f_{ij} is expected to be long-ranged with respect to the distance r_{ij} between sites i and j.

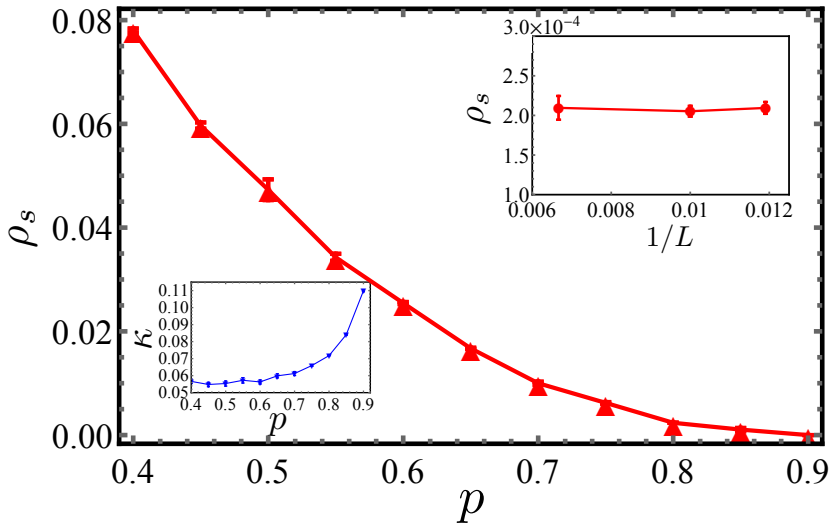

Figure 7.8: $V/J = 0$. Main plot, superfluid density ρ_s as a function of site-dilution p for $L = 84$. Superfluidity is strongly suppressed at larger site-dilution. Bottom-left inset, compressibility κ as a function of site-dilution p. Compressibility increases at large enough site dilution. Top-right inset, superfluid density ρ_s as a function of $1/L$ at site-dilution $p = 0.9$. Error bars are within the symbols if not shown in the figures.

Let us start by considering the case $V/J = 0$ where no diagonal interaction is

present. This corresponds to absence of external dc electric field in an experimental setup. Figure 7.8 shows superfluid density ρ_s as a function of site dilution p for system size $L = 84$. As expected, superfluidity is suppressed as site dilution increases. I have considered site dilution up to $p = 0.9$. Even at such large dilution value, superfluidity, though strongly suppressed, still persists as demonstrated in the top-right inset of Figure 7.8, where I plot ρ_s as a function of $1/L$ for $L = 84$, 100, 150 and $p = 0.9$ (ρ_s saturates to a finite value with increasing L). To further support this conclusion, in Figure 7.9, I plot f_{ij} as a function of the distance along the x-direction for system sizes $L = 84$, 100, and 150 and at fixed $p = 0.9$. The correlation function exponentially decays to a constant value different than zero. Dotted lines in the figure are the result of the exponential fit $a * e^{-x/\xi} + b$ with $b \neq 0$. Note that, the correlation length ξ increases with system size. These results strongly indicate that the system remains SF for arbitrarily large values of site dilution. This fact can be understood as follows. Since at $V/J = 0$ the corresponding clean system is in a SF phase, even for site dilution p larger than the percolation threshold $p_c = 0.407253$ [108], though SF islands within the lattice are disconnected, coherence between them is guaranteed by long-range hopping. As site dilution increases, the average distance between SF islands also increases thus suppressing coherence and superfluidity. I notice that, a suppressed SF density will result in a suppressed critical temperature for the SF to normal liquid transition at finite temperature.

Interestingly, as site dilution increases, compressibility also increases, as the bottom-left inset of Figure 7.8 shows. This can be understood in a similar

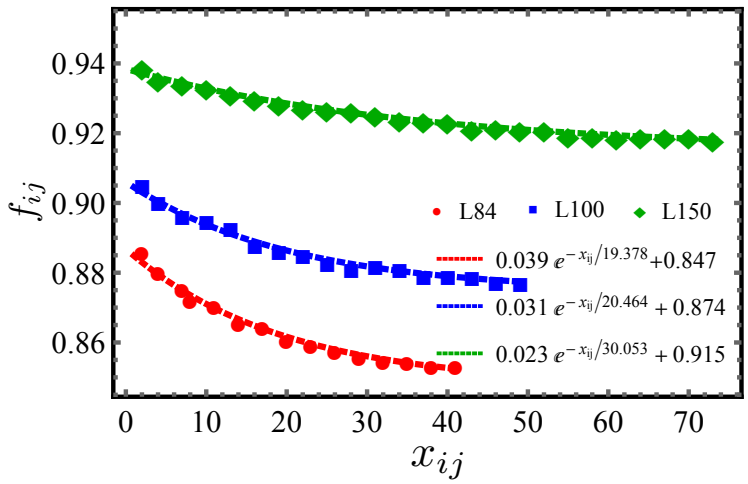

Figure 7.9: $V/J = 0$, $p = 0.9$. Correlation function f_{ij} as a function of the x-distance between sites i and j for system size $L = 84$, 100, and 150 (red circles, blue squares, and green diamonds, respectively). Dotted lines are the exponential fit $a * e^{-x/\xi} + b$. The correlation function decays to a constant value different than zero, suggesting the system is in a SF phase. Note also that the correlation function ξ increases with system size.

manner. Increased site-dilution corresponds to a larger average distance between disconnected lattice regions, making it harder for particles to delocalize within the entire lattice. This implies a non-uniform density distribution within the lattice and the presence of lower-density regions contributing to an increased compressibility. This can be seen in Figure 7.10 where I show the imaginary time average of the density distribution within the lattice for a single Monte Carlo configuration and a single dilution realization, at site dilution $p = 0.4$ (a) and $p = 0.85$ (b). The radius of a red circle at a given site is proportional to the density at that site. Blue dots represent sites which have been removed from the lattice. The standard deviation of the average density $n = 0.5$ corresponding to $p = 0.4$ and $p = 0.85$ are of the order of 0.045 and 0.1, respectively. The conspicuous presence of sites with significant lower than average density at $p = 0.85$

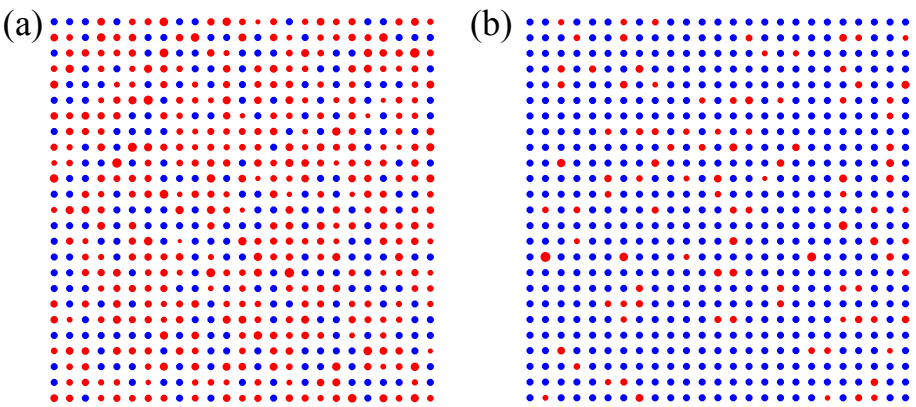

Figure 7.10: $V/J = 0$. Imaginary time average of the density distribution within the lattice for a single Monte Carlo configuration and a single dilution realization, at site dilution (a) $p = 0.4$ and (b) $p = 0.85$. The radius of a red circle at a given site is proportional to the density at that site. Blue dots represent sites which have been removed from the lattice.

is responsible for a larger compressibility. This scenario persists for configurations corresponding to larger and larger number of Monte Carlo steps. Once particles are able to reach a lower density region, they are "stuck" there due to suppressed hopping and the density distribution remains non-uniform.

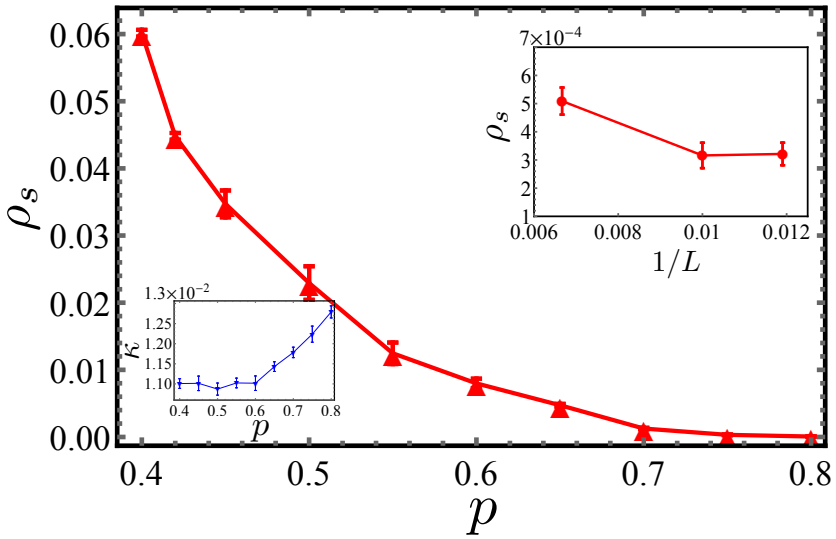

Figure 7.11: Same as Figure 7.8 but for $V/J = 7$ and $p = 0.75$.

At fixed interaction strength $V/J = 2$ and 7, I find qualitative similar results

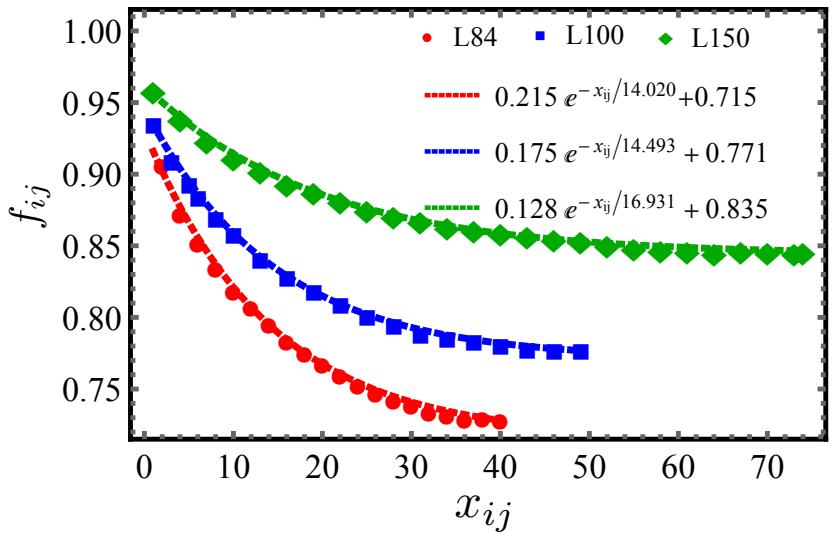

Figure 7.12: Same as Figure 7.9 but for $V/J = 7$ and $p = 0.75$.

as for $V/J = 0$. Here, I only report results corresponding to $V/J = 7$. Figure 7.11 shows superfluid density ρ_s as a function of site dilution p for $L = 84$. Superfluidity, though suppressed, remains finite even for large site dilution. The top-right insert of Figure 7.11 shows ρ_s increasing with system size at fixed $p = 0.75$, indicating that the system is SF. Figure 7.12 shows the decay of the correlator f_{ij} at $p = 0.75$ for system sizes $L = 84$, 100, and 150. As the exponential fit shows (dotted lines), the correlation function exponentially decays to a constant different than zero, with correlation length increasing with system size. These results imply that superfluidity, though suppressed, persists for large values of site dilution even at finite V/J. This can be understood as explained in the case of $V/J = 0$. As already observed for $V/J = 0$, which is shown in the bottom-left insert of Figure 7.11 in at large enough values of site dilution, compressibility increases. This increase is less dramatic than for $V/J = 0$ due to a finite value of interaction which suppresses density fluctuations.

7.6 Experimental realization

The model studied in this manuscript has been realized by loading KRb polar molecules into a deep optical lattice where hopping is suppressed. Molecules are cooled so that their hyperfine structures can be ignored. A spin 1/2 is encoded in the rotational degrees of freedom and microwave fields are used to induce transitions between two different rotational states. Spin interactions are directly driven by dipolar interactions without the requirement of particle tunneling. The ratio $J_\perp/J_z$ can be controlled by tuning the external dc electric field as well as by changing the choice of the rotational states which form the effective spin 1/2 system [114, 115]. For example, for rotational states used in Ref. [36], $J_z/J_\perp$ can be tuned from 0 to 3 using $\mathbf{E}$ fields from 0 to 16 kV/cm. Based on our results, for this experimental setup, only the easy-plane ferromagnetic order (equivalent to a superfluid phase of model (7.2)) may be observed. By choosing different rotational states [116], $J_z/J_\perp > 10$ can be achieved with similar $\mathbf{E}$ fields, so that easy-axis antiferromagnetic order (equivalent to checkerboard order) and the supersolid phase (where both easy-plane ferromagnetic and easy-axis antiferromagnetic order coexist) may be observed.

As for the site-diluted case, at the moment, filling factors achieved experimentally are $\lesssim 25\%$ corresponding to a site-dilution $p \gtrsim 0.75$ in model 7.2. At such large site-dilution, even for $J_z/J_\perp = 0$, the easy-plane ferromagnetic order is strongly suppressed. I have estimated that temperatures $T \sim 1.5$ nK are needed in order to observe easy-plane ferromegnetic order. Larger filling factors,

corresponding to smaller site-dilution, are a little more favorable for observing this phase. I have estimated that with site dilution $p = 0.5$, the easy-plane ferromagnetic order would be observed at temperature $T \sim 6.0$ nK.

7.7 Conclusion

Recent experiments with ultracold polar molecules trapped in deep optical lattices, where a spin 1/2 degree of freedom is encoded in two internal states, realize the site-diluted long-range XXZ model. Site dilution results in off-diagonal disorder. I have mapped the XXZ model onto the hard-core Bose-Hubbard model and have performed large-scale Monte Carlo simulations by the Worm algorithm. I have studied the ground state phase diagram of the model in the absence of site-dilution. I have found that, for large enough interaction, three phases are stabilized: a superfluid phase, a checkerboard solid phase, only present at density $n = 0.5$, and a checkerboard supersolid phase which can be reached by doping the CB phase away from half-filling. I have also studied the model in the presence of site-dilution and at fixed density $n = 0.5$. I have found that, unlike what observed in the case of short-range hopping, localization never occurs even for site dilution larger than the percolation threshold and off-diagonal order, though strongly suppressed, persists for arbitrarily large values of site-dilution. I have notice that, a suppressed SF density will result in a suppressed critical temperature for the SF to normal liquid transition at finite temperature, and have provided estimates for temperatures needed to observe coherence. Interestingly, I have found that

compressibility increases as site dilution increases.

Chapter 8

Conclusion

In this dissertation, I used the quantum Monte Carlo method by the Worm algorithm to study many-body bosonic lattice systems in the presence of disordered potential. I studied the ground-state phase diagram for three bosonic lattice systems: bosons in a quasi-periodic lattice, dipolar bosons in the presence of on-site random disordered potential, and the site-diluted long-range XXZ spin system, as realized by ultracold polar molecules, which can be mapped to a hard-core bosonic system in the presence of long-range hopping and long-range two-body interactions.

My work on two-dimensional bosons in quasi-periodic lattices provides the ground state phase diagram of this system. The ground state phase diagram contains three phases: superfluid, Mott insulator, and Bose glass. The finite temperature simulation results show that in the presence of quasi-periodic disordered potential, there is no Mott-glass-like Bose glass behavior separating the Mott insulator from the Bose glass, which is contrary to what was found in Ref. [81].

My work on the dipolar lattice bosons in the presence of random on-site diagonal disorder provides the ground state phase diagram at the fixed half-integer filling factor. The ground state phase diagram contains three phases: superfluid, checkerboard solid, and Bose glass. The results show that the interplay of the long-range interactions and the on-site disorder leads to suppression of the checkerboard phase, enhancement of the superfluid phase, and stabilization of the Bose glass

phase.

My work on the site-diluted long-range XXZ spin model provides the ground state phase diagram of the clean system in the absence of disorder. It also provides guidance for the experimentalists to find the superfluid phase for the system in the presence of site-dilution. The long-range XXZ spin model can be realized in experiments with ultracold polar molecules trapped in deep optical lattices. The site dilution, which results in off-diagonal disorder, corresponds to unoccupied sites in the experimental setup.

The systems studied in this dissertation can all be realized experimentally. The on-site contact interaction can be tuned by using Feshbach resonances and the long-range dipole-dipole interaction can be realized by using trapped ions, Rydberg atoms, highly magnetic atoms, and polar molecules. Disordered potentials can be generated using optical speckle patterns or bichromatic optical lattices. My theoretical work on these systems gives experimentalists insight into under which conditions certain phases can be reached experimentally. With continuous and rapid development of experimental techniques, one expects that these theoretical results may be tested in the near future.

References

[1] M. Greiner, O. Mandel, T. Esslinger, T. W. Hänsch, and I. Bloch, Nature **415**, 39 (2002).

[2] L. Fallani, C. Fort, and M. Inguscio, Adv. At. Mol. Opt. Phy. **56**, 119 (2008).

[3] B. Gadway, D. Pertot, J. Reeves, M. Vogt, and D. Schneble, Phys. Rev. Lett. **107**, 145306 (2011).

[4] W. Morong and B. DeMarco, Phys. Rev. A **92**, 023625 (2015).

[5] C. Fort, L. Fallani, V. Guarrera, J. E. Lye, M. Modugno, D. S. Wiersma, and M. Inguscio, Phys. Rev. Lett. **95**, 170410 (2005).

[6] G. Roati, C. D'Errico, L. Fallani, M. Fattori, C. Fort, M. Zaccanti, G. Modugno, M. Modugno, and M. Inguscio, Nature **453**, 895 (2008).

[7] V. Gurarie, L. Pollet, N. V. Prokof'ev, B. V. Svistunov, and M. Troyer, Phys. Rev. B **80**, 214519 (2009).

[8] L. Pollet, N. V. Prokof'ev, B. V. Svistunov, and M. Troyer, Phys. Rev. Lett. **103**, 140402 (2009).

[9] P. W. Anderson, Phys. Rev. **109**, 1492 (1958).

[10] P. A. Crowell, F. W. Vankeuls, and J. D. Reppy, Phys. Rev. Lett. **75**, 1106 (1995).

[11] P. S. Ebey, P. T. Finley, and R. B. Hallock, J. Low Temp. Phys. **110**, 635 (1998).

[12] T. Hong, A. Zheludev, H. Manaka, and L. P. Regnault, Phys. Rev. B **81**, 060410 (2010).

[13] R. Yu, C. F. Miclea, F. Weickert, R. Movshovich, A. Paduan-Filho, V. S. Zapf, and T. Roscilde, Phys. Rev. B **86**, 134421 (2012).

[14] R. Yu, L. Yin, N. S. Sullivan, J. S. Xia, C. Huan, A. Paduan, N. F. Oliveira, S. Haas, A. Steppke, C. F. Miclea, F. Weickert, R. Movshovich, E. D. Mun, B. L. Scott, V. S. Zapf, and T. Roscilde, Nature **489**, 379 (2012).

[15] H. S. J. Vanderzant, F. C. Fritschy, W. J. Elion, L. J. Geerligs, and J. E. Mooij, Phys. Rev. Lett. **69**, 2971 (1992).

[16] A. M. Goldman and N. Markovic, Phys. Today **51**, 39 (1998).

[17] R. Schneider, A. G. Zaitsev, D. Fuchs, and H. v. Löhneysen, Phys. Rev. Lett. **108**, 257003 (2012).

[18] J. E. Lye, L. Fallani, M. Modugno, D. S. Wiersma, C. Fort, and M. Inguscio, Phys. Rev. Lett. **95**, 070401 (2005).

[19] M. White, M. Pasienski, D. McKay, S. Q. Zhou, D. Ceperley, and B. DeMarco, Phys. Rev. Lett. **102**, 055301 (2009).

[20] F. Jendrzejewski, A. Bernard, K. Muller, P. Cheinet, V. Josse, M. Piraud, L. Pezze, L. Sanchez-Palencia, A. Aspect, and P. Bouyer, Nat. Phys. **8**, 398 (2012).

[21] L. Fallani, J. E. Lye, V. Guarrera, C. Fort, and M. Inguscio, Phys. Rev. Lett. **98**, 130404 (2007).

[22] T. Schwartz, G. Bartal, S. Fishman, and M. Segev, Nature **446**, 52 (2007).

[23] H. Hu, A. Strybulevych, J. H. Page, S. E. Skipetrov, and B. A. van Tiggelen, Nat. Phys. **4**, 945 (2008).

[24] P. A. Crowell, F. W. Van Keuls, and J. D. Reppy, Phys. Rev. B **55**, 12620 (1997).

[25] A. M. Goldman and N. Marković, Phys. Today **51**, 39 (1998).

[26] H. S. J. van der Zant, W. J. Elion, L. J. Geerligs, and J. E. Mooij, Phys. Rev. B **54**, 10081 (1996).

[27] B. Deissler, M. Zaccanti, G. Roati, C. D'Errico, M. Fattori, M. Modugno, G. Modugno, and M. Inguscio, Nat. Phys. **6**, 354 (2010).

[28] M. Pasienski, D. McKay, M. White, and B. DeMarco, Nat. Phys. **6**, 677 (2010).

[29] C. D'Errico, E. Lucioni, L. Tanzi, L. Gori, G. Roux, I. P. McCulloch, T. Giamarchi, M. Inguscio, and G. Modugno, Phys. Rev. Lett. **113**, 095301 (2014).

[30] A. Griesmaier, J. Werner, S. Hensler, J. Stuhler, and T. Pfau, Phys. Rev. Lett. **94**, 160401 (2005).

[31] T. Lahaye, T. Koch, B. Fröhlich, M. Fattori, J. Metz, A. Griesmaier, S. Giovanazzi, and T. Pfau, Nature **448**, 672 (2007).

[32] K. K. Ni, S. Ospelkaus, M. H. G. de Miranda, A. Pe'er, B. Neyenhuis, J. J. Zirbel, S. Kotochigova, P. S. Julienne, D. S. Jin, and J. Ye, Science **322**, 231 (2008).

[33] S. Ospelkaus, A. Pe'er, K. K. Ni, J. J. Zirbel, B. Neyenhuis, S. Kotochigova, P. S. Julienne, J. Ye, and D. S. Jin, Nat. Phys. **4**, 622 (2008).

[34] A. Chotia, B. Neyenhuis, S. A. Moses, B. Yan, J. P. Covey, M. Foss-Feig, A. M. Rey, D. S. Jin, and J. Ye, Phys. Rev. Lett. **108**, 080405 (2012).

[35] C.-H. Wu, J. W. Park, P. Ahmadi, S. Will, and M. W. Zwierlein, Phys. Rev. Lett. **109**, 085301 (2012).

[36] B. Yan, S. A. Moses, B. Gadway, J. P. Covey, K. R. A. Hazzard, A. M. Rey, D. S. Jin, and J. Ye, Nature **501**, 521 (2013).

[37] T. Takekoshi, L. Reichsöllner, A. Schindewolf, J. M. Hutson, C. R. Le Sueur, O. Dulieu, F. Ferlaino, R. Grimm, and H.-C. Nägerl, Phys. Rev. Lett. **113**, 205301 (2014).

[38] M. Lu, N. Q. Burdick, and B. L. Lev, Phys. Rev. Lett. **108**, 215301 (2012).

[39] K. Aikawa, A. Frisch, M. Mark, S. Baier, R. Grimm, J. L. Bohn, D. S. Jin, G. M. Bruun, and F. Ferlaino, Phys. Rev. Lett. **113**, 263201 (2014).

[40] K. Aikawa, A. Frisch, M. Mark, S. Baier, R. Grimm, and F. Ferlaino, Phys. Rev. Lett. **112**, 010404 (2014).

[41] J. W. Park, S. A. Will, and M. W. Zwierlein, Phys. Rev. Lett. **114**, 205302 (2015).

[42] A. Frisch, M. Mark, K. Aikawa, S. Baier, R. Grimm, A. Petrov, S. Kotochigova, G. Quéméner, M. Lepers, O. Dulieu, and F. Ferlaino, Phys. Rev. Lett. **115**, 203201 (2015).

[43] J. Billy, V. Josse, Z. Zuo, A. Bernard, B. Hambrecht, P. Lugan, D. Clément, L. Sanchez-Palencia, P. Bouyer, and A. Aspect, Nature **453**, 891 (2008).

[44] M. P. A. Fisher, P. B. Weichman, G. Grinstein, and D. S. Fisher, Phys. Rev. B **40**, 546 (1989).

[45] S. Rapsch, U. Schollwock, and W. Zwerger, Europhys. Lett. **46**, 559 (1999).

[46] W. Krauth, N. Trivedi, and D. Ceperley, Phys. Rev. Lett. **67**, 2307 (1991).

[47] S. G. Soyler, M. Kiselev, N. V. Prokof'ev, and B. V. Svistunov, Phys. Rev. Lett. **107**, 185301 (2011).

[48] F. Lin, E. S. Sørensen, and D. M. Ceperley, Phys. Rev. B **84**, 094507 (2011).

[49] C. Zhang, A. Safavi-Naini, and B. Capogrosso-Sansone, Phys. Rev. A **91**, 031604(R) (2015).

[50] A. E. Niederle and H. Rieger, New J. Phys. **15**, 075029 (2013).

[51] C. Zhang, A. Safavi-Naini, and B. Capogrosso-Sansone, Phys. Rev. A **97**, 013615 (2018).

[52] C. Zhang and B. Capogrosso-Sansone, Phys. Rev. A **98**, 013621 (2018).

[53] R. Grimm, M. Weidemüller, and Y. B. Ovchinnikov, Adv. At. Mol. Opt. Phy. **42**, 95 (2000).

[54] I. Bloch, Nat. Phys. **1**, 23 (2005).

[55] D. Jaksch, C. Bruder, J. I. Cirac, C. W. Gardiner, and P. Zoller, Phys. Rev. Lett. **81**, 3108 (1998).

[56] D. Jaksch and P. Zoller, Ann. Phys. **315**, 52 (2005).

[57] L. Pollet, C. R. Phys **14**, 712 (2013).

[58] A. Ghosal, M. Randeria, and N. Trivedi, Phys. Rev. Lett. **81**, 3940 (1998).

[59] Y. Dubi, Y. Meir, and Y. Avishai, Nature **449**, 876 (2007).

[60] M. Fisher, Phys. Rev. Lett. **65**, 923 (1990).

[61] M. Fisher, G. Grinstein, and S. Girvin, Phys. Rev. Lett. **64**, 587 (1990).

[62] J. D. Reppy, J. Low Temp. Phys. **87**, 205 (1992).

[63] K. Moon and S. Girvin, Phys. Rev. Lett. **75**, 1328 (1995).

[64] T. Giamarchi, C. Rüegg, and O. Tchernyshyov, Nat. Phys. **4**, 198 (2008).

[65] O. Nohadani, S. Wessel, and S. Haas, Phys. Rev. Lett. **95**, 227201 (2005).

[66] F. Yamada, H. Tanaka, T. Ono, and H. Nojiri, Phys. Rev. B **83**, 020409 (2011).

[67] E. Wulf, D. Hüvonen, J. W. Kim, A. Paduan-Filho, E. Ressouche, S. Gvasaliya, V. Zapf, and A. Zheludev, Phys. Rev. B **88**, 174418 (2013).

[68] O. Morsch and M. Oberthaler, Rev. Mod. Phys. **78**, 179 (2006).

[69] L. Sanchez-Palencia and M. Lewenstein, Nat. Phys. **6**, 87 (2010).

[70] J. W. Lee, M. C. Cha, and D. Kim, Phys. Rev. Lett. **87**, 247006 (2001).

[71] P. Schmitteckert, T. Schulze, C. Schuster, P. Schwab, and U. Eckern, Phys. Rev. Lett. **80**, 560 (1998).

[72] D. Boiron, C. Mennerat-Robilliard, J. M. Fournier, L. Guidoni, C. Salomon, and G. Grynberg, Eur. Phys. J. D **7**, 373 (1999).

[73] M. Segev, Y. Silberberg, and D. N. Christodoulides, Nat. Photon. **7**, 197 (2013).

[74] D. Clement, A. F. Varon, M. Hugbart, J. A. Retter, P. Bouyer, L. Sanchez-Palencia, D. M. Gangardt, G. V. Shlyapnikov, and A. Aspect, Phys. Rev. Lett. **95**, 170409 (2005).

[75] E. L. Pollock and D. M. Ceperley, Phys. Rev. B **36**, 8343 (1987).

[76] N. V. Prokof'ev, B. V. Svistunov, and I. S. Tupitsyn, J. Exp. Theor. Phys. **87**, 310 (1998).

[77] N. V. Prokof'ev, B. V. Svistunov, and I. S. Tupitsyn, Phys. Lett. A **238**, 253 (1998).

[78] N. Prokof'ev and B. Svistunov, arXiv: 0910.1393 (2009).

[79] M. E. J. Newman and G. T. Barkema, *Monte Carlo Methods in Statistical Physics* (Clarendon Press, United Kingdom, 1999).

[80] G. Roux, T. Barthel, I. P. McCulloch, C. Kollath, U. Schollwock, and T. Giamarchi, Phys. Rev. A **78**, 023628 (2008).

[81] Y. Wang, W. Guo, and A. W. Sandvik, Phys. Rev. Lett. **114**, 105303 (2015).

[82] X. L. Deng, R. Citro, E. Orignac, A. Minguzzi, and L. Santos, Phys. Rev. B **87**, 195101 (2013).

[83] Z. Yao, K. P. C. da Costa, M. Kiselev, and N. Prokof'ev, Phys. Rev. Lett. **112**, 225301 (2014).

[84] M. Nikolaou, M. Wallin, and H. Weber, Phys. Rev. Lett. **97**, 225702 (2006).

[85] K. R. A. Hazzard, B. Gadway, M. Foss-Feig, B. Yan, S. A. Moses, J. P. Covey, N. Y. Yao, M. D. Lukin, J. Ye, D. S. Jin, and A. M. Rey, Phys. Rev. Lett. **113**, 195302 (2014).

[86] A. De Paz, A. Sharma, A. Chotia, E. Marechal, J. H. Huckans, P. Pedri, L. Santos, O. Gorceix, L. Vernac, and B. Laburthe-Tolra, Phys. Rev. Lett. **111**, 185305 (2013).

[87] M. Lu, N. Q. Burdick, S. H. Youn, and B. L. Lev, Phys. Rev. Lett. **107**, 190401 (2011).

[88] M. Saffman, T. G. Walker, and K. Mølmer, Rev. Mod. Phys. **82**, 2313 (2010).

[89] R. Löw, H. Weimer, J. Nipper, J. B. Balewski, B. Butscher, H. P. Büchler, and T. Pfau, J. Phys. B: At. Mol. Opt. Phys. **45**, 113001 (2012).

[90] G. Gunter, H. Schempp, M. Robert-de Saint-Vincent, V. Gavryusev, S. Helmrich, C. S. Hofmann, S. Whitlock, and M. Weidemuller, Science **342**, 954 (2013).

[91] A. C. Potter, E. Berg, D.-W. Wang, B. I. Halperin, and E. Demler, Phys. Rev. Lett. **105**, 220406 (2010).

[92] B. Capogrosso-Sansone, C. Trefzger, M. Lewenstein, P. Zoller, and G. Pupillo, Phys. Rev. Lett. **104**, 125301 (2010).

[93] C. Zhang, A. Safavi-Naini, A. M. Rey, and B. Capogrosso-Sansone, New J. Phys. **17**, 123014 (2015).

[94] A. V. Gorshkov, S. R. Manmana, G. Chen, J. Ye, E. Demler, M. D. Lukin, and A. M. Rey, Phys. Rev. Lett. **107**, 115301 (2011).

[95] Z. X. Gong, M. F. Maghrebi, A. Hu, M. Foss-Feig, P. Richerme, C. Monroe, and A. V. Gorshkov, Phys. Rev. B **93**, 205115 (2016).

[96] Z. X. Gong, M. F. Maghrebi, A. Hu, M. L. Wall, M. Foss-Feig, and A. V. Gorshkov, Phys. Rev. B **93**, 041102 (2016).

[97] N. Y. Yao, C. R. Laumann, A. V. Gorshkov, S. D. Bennett, E. Demler, P. Zoller, and M. D. Lukin, Phys. Rev. Lett. **109**, 266804 (2012).

[98] X. Deng, R. Citro, E. Orignac, A. Minguzzi, and L. Santos, Phys. Rev. B **87**, 195101 (2013).

[99] D. Ceperley and E. Pollock, Phys. Rev. B **39**, 2084 (1989).

[100] J. M. Kosterlitz and D. J. Thouless, J. Phys. C: Solid State Phys. **6**, 1181 (1973).

[101] P. A. Crowell, F. W. Van Keuls, and J. D. Reppy, Phys. Rev. Lett. **75**, 1106 (1995).

[102] J. D. Reppy, B. C. Crooker, B. Hebral, A. D. Corwin, J. He, and G. M. Zassenhaus, Phys. Rev. Lett. **84**, 2060 (2000).

[103] S. A. Vitkalov, H. Zheng, K. M. Mertes, M. P. Sarachik, and T. M. Klapwijk, Phys. Rev. Lett. **87**, 251 (2001).

[104] L. S. Levitov, Phys. Rev. Lett. **64**, 547 (1990).

[105] P. Sengupta and S. Haas, Phys. Rev. Lett. **99**, 050403 (2007).

[106] N. Prokof'ev and B. Svistunov, Phys. Rev. Lett. **92**, 015703 (2004).

[107] T. Roscilde and S. Haas, Phys. Rev. Lett. **99**, 047205 (2007).

[108] T. Vojta, J. Crewse, M. Puschmann, D. Arovas, and Y. Kiselev, Phys. Rev. B **94**, 134501 (2016).

[109] S. A. Moses, J. P. Covey, M. T. Miecnikowski, B. Yan, B. Gadway, J. Ye, and D. S. Jin, Science **350**, 659 (2015).

[110] X. Deng, V. E. Kravtsov, G. V. Shlyapnikov, and L. Santos, Phys. Rev. Lett. **120**, 110602 (2018).

[111] X. Deng, B. L. Altshuler, G. V. Shlyapnikov, and L. Santos, Phys. Rev. Lett. **117**, 441 (2016).

[112] T. Matsubara and H. Matsuda, Prog. Theor. Phys. **16**, 569 (1956).

[113] V. G. Rousseau, Phys. Rev. B **90**, 134503 (2014).

[114] M. L. Wall, K. R. A. Hazzard, and A. M. Rey, arXiv: 1406.4758 (2014).

[115] B. Gadway and B. Yan, J. Phys. B: At. Mol. Opt. Phys. **49**, 152002 (2016).

[116] K. R. A. Hazzard, S. R. Manmana, M. Foss-Feig, and A. M. Rey, Phys. Rev. Lett. **110**, 075301 (2013).